DOI: 10.1002/ ((please add manuscript number))
Article type: Review

Engineering Local Coordination Environments of Atomically Dispersed and Heteroatom-coordinated Single Metal Site Electrocatalysts for Clean Energy-Conversion

Yuanzhi Zhu, Joshua Sokolowski, Xiancheng Song, Yanghua He, Yi Mei, and Gang Wu**

Dr. Y. Zhu, X Song, Prof. Y. Mei
Faculty of Chemical Engineering, Yunnan Provincial Key Laboratory of Energy Saving in Phosphorus Chemical Engineering and New Phosphorus Materials, The Higher Educational Key Laboratory for Phosphorus Chemical Engineering of Yunnan Province, Kunming University of Science and Technology, Kunming 650500, China.
E-mail: meiyi412@126.com;

J. Sokolowski, Y. He, Prof. G. Wu
Department of Chemical and Biological Engineering, University at Buffalo, The State University of New York, Buffalo 14260, New York, United States
Email: gangwu@buffalo.edu

Keywords: electrocatalysis, energy conversion, single-atom site catalysts, heteroatom doping, coordination environment

Carbon-based heteroatom-coordinated single-atom catalysts (SACs) are promising candidates for energy-related electrocatalysts because of their low-cost, tunable catalytic activity/selectivity, and relatively homogeneous morphologies. The unique interactions between single metal sites and surrounding coordination environments play a significant role in modulating the electronic structure of the metal centers which could lead to unusual scaling relationships, new reaction mechanisms, and improved catalytic performance. This review summarizes the recent advances in engineering the local coordination environment of SACs for improved electrocatalytic performance for several crucial energy-convention electrochemical reactions: oxygen reduction reaction, hydrogen evolution reaction, oxygen evolution reaction, CO_2 reduction reaction, and

nitrogen reduction reaction. Various engineering strategies including heteroatom-doping, changing the location of SACs on their support, introducing external ligands, and constructing dual metal sites are comprehensively discussed. The controllable synthetic methods and the activity enhancement mechanism of state-of-the-art SACs are also highlighted. Recent achievements in the electronic modification of SACs will provide an understanding of the structure-activity relationship for the rational design of advanced electrocatalysts.

1. Introduction

Renewable energy generation (*e.g.*, wind, sun, and tidal energy) is a promising alternative to fossil fuel consumption as it has the potential to meet the ever-increasing energy demand while simultaneously mitigating environmental issues.[1, 2] In order to minimize the inherent weaknesses of these technologies, such as fluctuation and intermittency, development of advanced energy conversion technologies is indispensable. In an energy cycle driven by renewable sources, electricity is first converted into chemical energy in the form of H_2 and O_2 through water splitting, utilizing electrochemical reactions such as the hydrogen evolution reaction (HER) and oxygen evolution reaction (OER).[3, 4] Then, the generated H_2 and O_2 are converted back to water in fuel cells, through the oxygen reduction reaction (ORR), regenerating the electricity.[5, 6] The discharging and charging processes in rechargeable metal–air batteries are driven by the ORR and OER.[7] Other electrochemical reactions, namely the CO_2 reduction reaction (CO_2RR) and nitrogen reduction reaction (NRR), enable the utilization of N_2 and CO_2 to produce fuels or value-added

products.[8] However, these processes are generally hampered by sluggish reaction kinetics and need efficient electrocatalysts to facilitate these reactions.[9]

Single-atom catalysts (SACs) have recently attracted interest because of their maximum atomic utilization efficiency and high mass activity.[10] Among them, the MN_xC_y (M= Pt, Ru, Fe, Co, etc.) moieties with isolated metal atoms coordinated by intrinsic defects or heteroatoms on carbon-based substrates have been extensively explored as efficient electrocatalysts for many electrochemical reactions.[11] The carbonaceous substrates (amorphous carbon, graphene, carbon nanotubes, g-C_3N_4, etc.) not only have high electrical conductivity for fast electron transport, but also large specific surface area to prevent metal agglomeration via the strengthened metal-support interaction.[12-14] These interactions play a key role in tuning the charge density and the d orbital states of the metal active sites, enabling optimization of the adsorption energy for the intermediates on the metal surface. As the metal active sites decrease in size to the atomic level, their sensitivity to the support becomes maximal. Consequently, the change in local coordination environment may lead to the emergence of new catalytic active sites and reaction pathways, further enhancing the catalytic performance. Influencing the local atomic environment through factors including the location (edge or in-plane), surrounding heteroatoms, grafting additional ligands on metal center, and creating dual-metal sites have been demonstrated to be effective methods to enhance the activity of SACs for many energy-related electrocatalytic reactions. Although some excellent review articles have focused on the importance of metal–support interactions or defects for the rational design of SACs,[8, 15, 16] the effect of the local coordination environment on the

electrochemical performance of carbon-based heteroatom coordinated SACs has not been systematically summarized.

In this review, we first emphasize the significant role of coordination for stabilizing and improving SACs and discuss computational studies on SACs to provide knowledge of the relationship between the local coordination environment and the activity of SACs. Then, synthetic strategies that are effective for preparing SACs with tunable electronic structures are summarized. Finally, potential applications of SACs in challenging electrochemical reactions including the ORR, HER, OER, CO_2RR, and NRR are discussed. Compared to other published reviews, we mainly focus on recent advancements in engineering local coordination environments and their mechanisms with an aim to improve catalyst performance.

2. Coordination-based single metal sites

2.1 The role of coordination in stabilizing single metal sites

Since single metal atoms have high surface energies, they tend to agglomerate and usually need to be anchored onto substrates via strong coordination bindings to maintain atomic dispersion during the synthetic and catalytic processes. Many types of defects or heteroatoms on carbon-based substrates such as single vacancy (SV) defects,[17] double vacancy (DV) defects,[18] edge,[19] pyridine-type N,[20] pyrrole-type N,[21] and thiophene-type S[22] have been reported as effective coordination sites to stabilize various single atoms. For example, theoretical calculations revealed that Pt single atoms anchored on vacancies and edges of the graphene support are more stable than the corresponding Pt dimers and inhibit the formation of the Pt cluster during the water activation

process.[23] At elevated temperatures, above 900 ºC, the noble metal nanoparticles (Pd, Pt, Au) could be transformed to thermally stable single atoms coordinated by four N atoms (MN_4) with a formation energy of –3.96 eV.[24]

Although the activity of SACs largely originates from the adsorption/desorption of intermediates onto the metal center with unsaturated d orbital, the local coordination environment of the support also plays an important role in controlling activity and selectivity. The charge transfers and redistribution between the metal atom and surrounding coordinating atoms could modulate the electronic structure of SACs to optimize the adsorption properties, implying the possibility of engineering the local coordination environment of SACs for improved catalytic activity.

2.2 Determination of coordination-based single metal sites

In order to characterize heteroatom-coordinated SACs in terms of their geometric configuration and electronic structures, advanced characterization techniques have been employed. For instance, scanning transmission electron microscopy (STEM) can visualize the atomically dispersed metal atoms and distinguish it from metal particle aggregates.[20] It offers useful information to study the particle size distribution as well as the coordination configuration of the SACs on the carbon-based supports, due to the obvious difference in contrast between metal atoms and light elements. The *in-situ* STEM technology has been used to observe the evolution process of the SACs from bulk metals.[24] However, STEM technology does not provide the information about electronic interactions between metal centers and the coordination environment. The high-energy electron

beam of STEM might damage the carbon-based support, especially the amorphous carbonaceous structure with relatively poor stability, which makes some defect or edge-hosted SACs hard to observe.[25]

X-ray absorption spectroscopy (XAS) analysis, including the extended X-ray absorption fine structure (EXAFS) and X-ray absorption near edge structure (XANES) spectra, is an important tool to reveal the electronic state, local geometric structure, and charge transfer trend of SACs.[26, 27] The XANES can provide information on the oxidation state and coordination symmetry of SACs due to its sensitivity to the charge states of the metals and surrounding coordination atoms. The EXAFS is sensitive to the local structure without the need of long-range order, thus it can provide information about the coordination number and bond distance of the SACs. The X-ray photoelectron spectroscopy (XPS) can also reflect the oxidation states, chemical environments, and bonding information of the metal centers and its surrounding heteroatoms (e.g. N and S) which is usually used to supplement and support the results of XAS analysis.[28, 29] For Fe-based SACs, the ^{57}Fe Mössbauer spectroscopy is a fingerprint technique that reflects the local electronic structure and coordination state of the Fe metal center.[30, 31] Considering the complex structure of carbon-based SACs, a combination of the above-mentioned technologies is desired to achieve relatively accurate conclusions.

The structures of SACs derived from the spectra can be used for density functional theory (DFT) calculations. The DFT calculations[32] could provide quantitative information about the charge density distribution, spin distribution, the density of the state of the hybrid orbital, and the

adsorption energy of the reaction intermediates for SACs, all of which are important parameters for the rational design of SACs for various electrocatalytic reactions.

3. Computational insight into the structure-activity correlation for SACs

Although it is well established that the local coordination environment could modulate the electronic structure of the metal center, how the properties of the coordination atoms, including atomic type, configuration, electronegativity, and coordination number, affect the electrocatalytic activity of SACs remain elusive. Consequently, trial-and-error approaches are commonly adopted to maximize performance of SACs. For rational design, an in-depth study on the structure-activity relationship of SACs is highly desired. In this regard, DFT calculations have driven important developments in understanding the origins of electrocatalytic activity and establishing guiding principles for the design of carbon-based SACs.

According to the Sabatier principle, an ideal catalytic site should bind the reaction intermediates neither too weakly nor too strongly.[33] This phenomenon has been cast into an intuitive tool, volcano plots, which pictorially characterizes catalytic activity with respect to catalyst-intermediate interactions. Based on the volcano plots, a simplified activity description, associated with intrinsic structural properties of the SACs, could be established (**Figure 1**). It can provide fundamental insight into how the local coordination environment of the single metal center controls the adsorption strength, further guiding the engineering of SACs to improve their electrocatalytic performance.

3.1 Descriptors for oxygen involved electrocatalysis

The O_2 involved ORR and OER processes usually involve the adsorption/desorption of O_2^*, OOH*,

O*, and OH* reaction intermediates on the SACs surface. Taking the ORR as an example, the four-electron reaction can follow either an associative or a dissociative mechanism.[34] Considering the relatively high oxygen dissociation ($O_2 + 2^* \rightarrow 2O^*$) barrier on MN_x sites, some studies suggest that the ORR more readily follows the associative mechanism. The simplified associative ORR mechanism in acidic environment is given in Equation (1–5):[35, 36]

$$\text{Associative: } O_2 + * \rightarrow O_2^* \qquad (\Delta G_1) \qquad (1)$$

$$O_2^* + H^+ + e^- \rightarrow OOH^* \qquad (\Delta G_2) \qquad (2)$$

$$OOH^* + H^+ + e^- \rightarrow O^* + H_2O \qquad (\Delta G_3) \qquad (3)$$

$$O^* + H^+ + e^- \rightarrow OH^* \qquad (\Delta G_4) \qquad (4)$$

$$OH^* + H^+ + e^- \rightarrow H_2O + * \qquad (\Delta G_5) \qquad (5)$$

where * represents a catalytic active site. Considering the difference in adsorption free energy (ΔG_{ads}) of the intermediates, the overpotential for the ORR/OER actually depends on the free energy variation (ΔG) of the potential-determining step with the highest energy barrier. The ΔG_{ads} for O* (ΔG_{O*}) and OH* (ΔG_{OH*}) have been used as activity descriptors of MN_x or MC_x based SACs for ORR and OER[37-39] mainly for the purpose of fast screening and rational design of new SACs. However, they are not related to the intrinsic structural characteristics of the active centers.

The first descriptor, the Lewis basicity of the carbon-based substrates, was provided by Ramaswamy and co-workers who could correlate the activity of FeN_4 sites with the degree of π-electron delocalization.[40] It was proposed that the activity of FeN_4 is limited by the strong chemisorption bond strength of the ORR intermediates. The highly disordered carbon substrates

with stronger electron withdrawing capability facilitate the weakening of the adsorption energy by downshifting the energy level of the e_g-orbital (d_z^2) of the Fe center, thus achieving enhanced activity. However, this descriptor cannot provide reaction kinetics such as the effect of the potential-determining step on the ORR activity. Recently, Xu *et al.* discovered a universal activity descriptor (φ) for graphene-based SACs that directly correlates the ORR/OER activities with the coordination configurations.[41] They first studied the linear relationships between different intermediates (Figure 1a) and produced an activity volcano curve with ΔG_{OH*} as the descriptor (Figure 1b). A new linear relationship between φ and ΔG_{OH*} was successfully established by considering several electronic structure based parameters of the active sites (Figure 1c) including valence electrons in the occupied *d* orbital (θ_d) of the metal centers, electronegativity of the coordination atoms, and the coordination number. According to the expression of φ, the local coordination environment, which endows metal centers with more valence electrons in the *d* orbital after charge redistribution, leads to weaker adsorption of intermediates on SAC sites, and vice versa. The Fe-pyridine-N_4, Co-pyridine-N_4, and Fe-pyrrole-N_4 are predicted to be ORR active sites, consistent with common experimental observations (Figure 1d).

The reaction pathway for the CO_2RR is more complex than the electrocatalytic ORR and OER. It can produce the C_1 (e.g., CO and formic acid), C_2 (e.g. ethylene and ethanol) and C_3 products (e.g., propyl alcohol and acetone).[42, 43] Due to the variety of the intermediates involved, establishing suitable descriptors to guide the design of SACs for CO_2RR remains a grand challenge. For electroreduction of CO_2 to CO, which involves *CHO/COOH* and *CO as intermediates, the

scaling relation between *CHO and *CO obviously deviates from linearity for graphene supported SACs, probably due to a strong electronic interaction between the d-orbital of the metal atom and the p-orbital of graphene.[44] Recently, Gong et al.[45] employed the ΔG_{*CO} as a descriptor to build a volcano plot for porphyrin-based SACs. Moreover, they established a new descriptor (Φ) that associates the intrinsic CO_2RR activity of porphyrin-based SACs with the electronegativity of the metal atoms. The Co porphyrin is predicted to be the best catalyst, among other non-precious analogues, which is in agreement with experimental results.

3.2 Descriptors for hydrogen involved electrocatalysis

The HER process in acidic media can occur through either the Volmer–Heyrovsky mechanism ($H^+ + e^- + * \rightarrow H^*$; $H^* + H^+ + e^- \rightarrow H_2 + *$) or the Volmer–Tafel mechanism ($H^+ + e^- + * \rightarrow H^*$; $2H^* \rightarrow H_2 + 2*$). As the HER only involves one intermediates (H*), ΔG_{H^*} has been widely used as the descriptor for MN_x or MC_x sites on graphene substrates. According to DFT calculations, single-coordinated Ni atoms on zigzag edge,[37] single vacancy,[17] and topological defects *(e.g.*, 5775 defect)[18] of undoped graphene exhibit ΔG_{H^*} values close to zero, which allows for maximal HER activities. In addition, the ΔG_{H^*} value was found to be very sensitive to the d-band center of the metal atoms. For example, the d-band center of Ni shifts deeper with respect to the Fermi level when the coordination number increases, this is accompanied by weaker binding strength of H*.[37] The activity–electronic structure relationship for a series of transition metal based MN_4 sites (Co, Fe, Ni, Mn, Mo, W, Pd, Ru, etc.) was studied by Hossain and co-workers.[46] The DFT results reveal that the ΔG_{H^*} is highly related to the energy states of the d_z^2 valence orbitals, and their

resulting antibonding orbitals (σ*), after H adsorption. Higher energy levels of σ* induce a more unoccupied orbital, resulting in stronger adsorption of H* intermediates and vice versa. Thus, CoN_4 moieties with neither completely empty, nor fully filled, antibonding orbitals exhibited an ideal ΔG_{H^*} resulting in superior HER activity. This result was confirmed by experimental results.

The NRR is a multi-electron transfer reaction that involves multiple intermediates (e.g., NNH*, NNH_2*, N*, NH*, and NH_2*). Recently, Liu et al. presented a systematic computational study on the NRR activity (Figure 1e) and stability (Figure 1f) of N-coordinated SACs with various transition metal centers anchored on the g-C_3N_4 and other two N-doped carbon substrates.[47] The adsorption energy of N* (ΔE_{N^*}) was found to scale linearly with ΔE_{NNH^*} and ΔE_{NH2^*} and, thus, could serve as an activity descriptor for the NRR. The variation of ΔE_{N^*} was attributed to the influence of metal centers on the bonding/antibonding orbital populations. Different substrates affect the NRR activity and stability by introducing different ligand effects. According to the calculation results, Ru atoms anchored on g-C_3N_4 were predicted to be promising NRR electrocatalysts with acceptable Faradaic efficiency (FE) and stability. The Co and W based samples showed good activity for the NRR, however, the HER is more likely to occur within the same working potential windows, leading to low selectivity for the NRR on these sites.

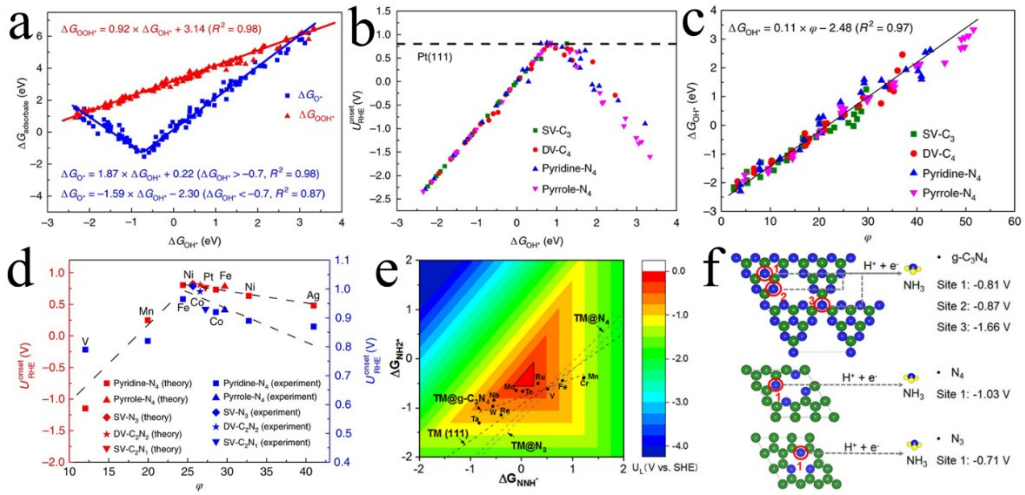

Figure 1. (a) The scaling relations between ΔG_{OOH*}, ΔG_{O*} and ΔG_{OH*} for metal atoms with diverse configuration. (b) The theoretical onset potential for ORR versus the descriptor ΔG_{OH*}. (c) The linear relationship between ΔG_{OH*} and the descriptor φ. (d) The theoretical and corresponding experimental overpotentials for ORR versus the descriptor φ. Reproduced with permission.[41] Copyright 2018, Springer Nature. (e) The color contour plots of the limiting potential versus adsorption strength of *NNH (ΔG_{NNH*}) and *NH_2 (ΔG_{NH2*}). (f) Decomposition energies of g-C_3N_4 and other N-doped substrates, suggesting their stability under moderate reduction potentials. Reproduced with permission.[47] Copyright 2019, American Chemical Society.

4. Engineering SACs on carbon-based substrates

The previous section provides theoretical guidance for designing heteroatom-coordinated SACs as efficient electrocatalysts. Improvement in the activity of SACs, which mainly originates from the optimized adsorption energy of the rate-controlling reaction intermediates, is a direct result of the charge redistribution between the metal center and the surrounding coordination atoms that

modulate their electronic structure. The challenge is accurate implementing the expected electronic structural modulation of SACs through innovative material design. As revealed by theoretical predictions and experimental results, changing the metal center is a relatively simple method to tune the activity and selectivity of SACs, such as in the case of the ORR[48, 49] and OER.[20] This could be readily achieved by choosing different metal precursors during SAC synthesis. However, this strategy has intrinsic limitations with respect to the degree of adjustment due to the limited metal types. Engineering the local coordination environment could be another effective route to enhance the performance of SACs. Due to their tunable structures, morphologies, sizes, degrees of π-electron delocalization, and heteroatom dopants, carbon-based substrates are ideal for regulating the electronic structure of SACs. As shown in **Figure 2**, several regulation strategies have been proposed to realize the charge redistribution of SACs including heteroatom doping, changing the location of SACs, introducing external ligands on the metal centers, and constructing dual-metal sites. In the following section, we summarize the underlying mechanisms that lead to this charge transfer induced activity enhancement.

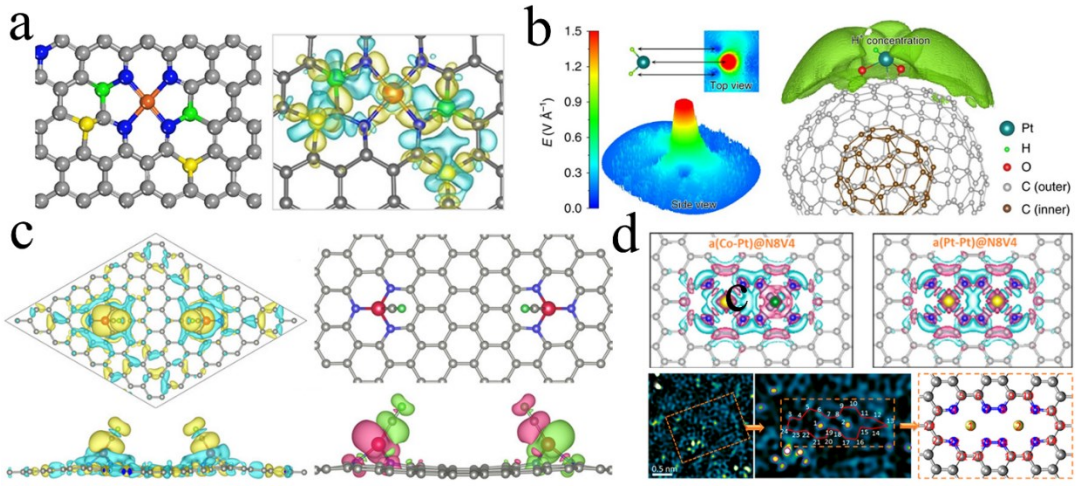

Figure 2. (a) The charge density redistribution induced by S, P doped FeN_4 sites on a graphene substrate. Gray, blue, orange, yellow and green represent the C, N, Fe, S and P atoms, respectively. Yellow and blue areas represent charge accumulation and depletion, respectively. Reproduced with permission.[50] Copyright 2018, Springer Nature. (b) The electric field distribution (left) and proton concentration distribution (right) of the tip-like Pt atomic site on highly curved fullerenes-like supports. Reproduced with permission. [51] Copyright 2019, Springer Nature. (c) The CO-induced charge density difference (left) and net spin density (right) of two adjacent FeN_3 sites on a graphene substrate. Yellow and blue bubbles represent charge accumulation and depletion, respectively. Reproduced with permission.[52] Copyright 2018, American Chemical Society. (d) The charge density distributions of the dual Co-Pt sites (top left) and the Pt-Pt control (top right) and the HAADF image of Co-Pt sites (bottom). Reproduced with permission.[53] Copyright 2018, American Chemical Society.

4.1 Heteroatom doping

Heteroatom doping involves the substitution of carbon atoms within the carbon skeleton.

Heteroatoms with a different size and electronegativity induce a charge redistribution at the metal center by either directly acting as a coordination atom (e.g., PtS_4[22] or NiN_3S[54]) or modulating the long-range electronic structure of the support.[55]

For N-coordinated SACs, such as the widely studied MN_x sites, the role of N heteroatoms on carbonaceous substrates is not only to anchor metal atoms, but also to modulate their electronic properties. The electron-withdrawing/donating character of N dopants varies with the N-configuration. The electron on quaternary/pyrrole N was found to delocalize into the surrounding C atoms to give an n-type doping while the pyridine-type N usually led to a p-type doping.[56, 57] Therefore, the contributions to the charge redistribution of the SACs should also be different. For example, several recent studies proposed that the pyrrole-type FeN_4 configurations,[21, 58] rather than the earlier accepted pyridine-type configurations,[59] were responsible for the high ORR activity. Pyrrole-type FeN_4 could further trigger the synergistic effect to activate surrounding C atoms whereas pyridine-type FeN_4 cannot.[58] For the OER, the well-defined structure and high activity of several pyridine-type MN_4 (M= Ni, Co, Fe) have been experimentally verified.[20] Similarly, the coordination number of C-coordinated SACs (MC_x) determines the adsorption strength of the intermediates and leads to different catalytic behaviors. The Ni atoms located on 5775 defects are more active for the HER while the Ni atoms on divacancy defects are favorable for the OER.[18] The contribution of N atoms that do not participate in coordination cannot be ignored. Higher pyrolytic temperatures (up to 1100 °C) help to generate MN_4 (M= Co, Fe) sites that likely facilitate the formation of more graphitic N components for better conductivity, thus

resulting in enhanced ORR activity.[60, 61] The FeN_4 moieties pyrolyzed under an NH_3 atmosphere were found to exhibit much higher ORR activity than ones under an Ar atmosphere, most likely resulting from the increased basicity of the carbon-based substrate caused by N doping.[21]

Diverse heteroatom dopants in carbon substrates could further modulate the electronic structure of SACs. Recently, several groups have synthesized S, B, P and S/P doped MN_x (M= Fe and Ni) sites resulting in improved ORR, HER, and OER performance.[8] However, the effect of the charge redistribution induced by heteroatom doping on the adsorption energy of intermediates remains elusive. Due to complex heteroatom coordination effects and uncertain scaling relations for SACs, establishing guidelines for the rational design of heteroatom-doped SACs remains a challenge if only based on the intrinsic electronic properties of heteroatoms. Some works have adopted the electronegativity of dopants as an index to analyze the trends of the electronic delocalization and to account for the improved electrocatalytic performance after heteroatom doping.

4.2 Local environments of single-atom sites

Given identical geometric configurations, the activity of SACs also depends on their location on the supports. Due to the existence of dangling bonds, the coordinating atoms at the edge behave differently to those in-plane ones in terms of their effect on metal atom sites. DFT calculations indicate that the proportion of edge-hosted Fe_xN_y moieties might be larger than the bulk-hosted ones due to lower formation energies. However, they are not easily observed by using STEM because of their relatively poor stability when exposed to the electron beam.[25] The edge-N atoms with dangling bond defects could improve the adsorption of intermediates during the rate-

determining step by affecting the charge density distribution of the FeN_4 sites, resulting in higher activity.[19] For instance, two configurations of MN_4 sites were proven active for the ORR. One is the edge-hosted MN_{2+2} sites bridging over two adjacent armchair graphitic edges and the other is in-plane MN_4 embedded in an intact graphitic layer. DFT investigations revealed that the FeN_4 or CoN_4 sites on a basal plane may not facilitate the reaction on a dissociative ORR pathway because some intermediate steps are endothermic processes (e.g., the dissociation of *OOH to *O and *OH).[62, 63] However, edge-hosted FeN_{2+2}[64] or CoN_{2+2} [65]sites could synergize with adjacent pore defects or C vacancies with dangling bonds to reduce reaction barriers for the ORR and CO_2RR, leading to an enhanced thermodynamic limiting potential. In addition, the SACs on edges are more easily accessible to reactants, which is beneficial for mass transfer. In a work with FeN_x sites supported on graphite, a negative correlation between the number of graphitic layers and fuel cell performance was observed, implying that FeN_x sites within the graphitic plane also highly contributes to the catalytic activity.[66] Similar to the configurations at the edges, Pt atoms anchored on highly curved supports exhibited excellent HER activity.[51] The high curvature of the support could lead to the accumulation of electrons around the Pt regions, which induces a local electric field for proton (H^+) enrichment, thus accelerating the catalytic kinetics (Figure 2b).

4.3 Dual metal site synergy

Dual metal sites can be regarded as a derivative structure of SACs with two different kinds of MN_xC_y sites located adjacently in the same substrate with definite intermetallic interaction and charge polarization (Figure 2d). These sites usually exhibit synergetic effects. Several dual metal

sites have demonstrated their superiority in energy-related electrocatalysis including N-coordinated Co-Fe,[67-70] Co-Pt,[53] Zn-Co[71, 72] and Fe-Mn[73] for the ORR, Co-Pt[74] and Pt-Ru[75] for the HER, and Fe-Ni for the CO_2RR.[76]

Compared to metal-free heteroatom sites, synthesis strategies generally lead to an improvement in intrinsic activity of the SACs rather than the introduction of new active sites. This situation is different if a second transition metal atom is introduced as a promoter. First, the d-d orbital hybridization between two single metal sites, different than p-d orbital hybridization between metals and N or other metal-free heteroatoms, provides a new opportunity to modulate electronic structure.[75] Both metal sites can serve as active centers after undergoing charge redistribution, which not only increases the atomic utilization, but also leads to new reaction pathways with lower reaction barriers. For example, theoretical predictions revealed that the most kinetically favorable reaction pathway for the ORR on FeN_4 would be a four-electron dissociation pathway, in which the rate-determining step involves the dissociation of OOH* into O* and OH*.[62] The dual Co-Fe active center could provide two adjacent adsorption sites for dissociated O* and OH* intermediates, thus decreasing the dissociation barrier of OOH* and enhancing ORR activity.[68] Similar enhancement mechanisms have also been proposed for CO_2RR on N-coordinated Ni-Fe sites.[76]

4.4 Grafting external ligands onto the metal center

Introducing external coordination atoms beyond the substrate is another effective strategy to engineer the local coordination environment of SACs. Previous studies revealed that the adsorption of *OH from water activation on the FeN_x sites does not poison the Fe center, but instead acts as

an axial modifying ligand to optimize the binding energies of O_2 and corresponding intermediates, leading to new active sites that have higher ORR catalytic activities.[77-79] Similarly, operando experiments and DFT calculations suggest that a CO ligand does not poison atomic PtS_3 sites as it does bulk Pt metal.[80] Instead, it makes the Pt atom more electrophilic via the metal-to-ligand charge transfer which facilitates the H* formation via water dissociation, enhancing the HER kinetics. An additional pyridine ligand could also favorably modulate the interaction strength of oxygen intermediates on the FeN_4 sites, thus boosting the ORR activity.[81] Zeng et al. reported the modification of FeN_4 sites via grafting a Pt_1–O_2– ligand onto the Fe center.[82] The induced Pt_1–O_2– ligands probably have multiple roles throughout the electrocatalytic reaction, including modulating the electronic structure of FeN_4 for optimized adsorption energy of intermediates, acting as a new active center to synergize with FeN_4 sites by facilitating the H_2O dissociation, and preserving the FeN_4 sites from being attacked by H_2O_2, thus simultaneously enhancing the catalytic performance of the ORR, OER and HER. Han et al. revealed that the d band structure of FeN_4 sites on S-doped carbon could be tuned by inducing an axial Cl ligand, leading to an optimized O_2 binding energy that enhances ORR activity.[55] The coordination number of Cl atoms was also found to affect the HER activity of graphdiyne supported Pt SACs.[83] The reduction of the external Cl coordination number from four to two could weaken the H* to obtain a ΔG_{H^*} close to zero for improved HER activity.

In addition to tuning charge density, the difference in spin density is also significant for activity enhancement.[84] Recently, DFT calculations revealed that the adsorption of CO on the Fe atom

center could trigger cooperative interactions between two nearby FeN_3 sites on graphene, which not only induces a charge redistribution, but also leads to a unique long-range spin coupling effect (Figure 2c).[52] These findings imply that the electronic properties of SAC sites could be further regulated by combining increased atomic distribution density and introduction of external coordination atoms.

5. Innovative synthesis of SACs on carbon substrates

Diverse strategies for atomically dispersing metal sites on carbon-based substrates have emerged and have also been summarized by several SAC related reviews, but these works mainly focused on achieving densely dispersed single-atomic sites or on improving the morphologies of the substrates to facilitate mass transfer. Efficient and precise engineering of SACs with tunable local coordination environments remains a grand challenge. In this section, instead of providing a comprehensive summary of the available methods, we review synthetic strategies to fabricate novel and tunable SAC structures.

5.1 Thermal conversion from structurally defined MOF precursors

Metal organic frameworks (MOFs) are unique materials with ultrahigh porosity, tunable components and pore sizes, and well-defined crystalline architectures. Different from the physical mixture of N-, C-, and metal-containing small molecules, the MOF skeleton allows the pre-arrangement of N, C, and metal elements at the molecular level. This skeleton can then act as a template for the formation of ordered carbonized derivatives with uniformly dispersed SAC sites.[85-87] Pyrolysis of Zn-based bimetallic MOFs (usually Co, Fe, Ni, etc. modified ZIF-8) has

become the most popular synthetic method for MN_xC_y moieties, where the imidazole ligand of ZIF-8 serves as the necessary C and N source.[88, 89] The target metal resource could be anchored on the node through partial substitution of the Zn atom, adsorbed onto the functional groups of the ligand, or confined within a cavity during MOFs synthesis. During pyrolysis, the evaporation of Zn not only produces free N sites to stabilize the nonvolatile target metal atom, leading to highly dispersed SACs sites, but also generates sufficient pores and surface area.[89]

Effect of pyrolytic temperature. The density and the intrinsic activity of MN_4 sites in MOF derived catalysts are primarily dependent on heating temperatures. 800 °C was experimentally proven to be the minimum temperature for yielding active FeN_4 and CoN_4 sites.[60, 61] Higher temperatures can lead to a more complete volatilization of the Zn element, resulting in higher surface area and more exposed active sites. The N coordination number of MN_x sites also varies with temperature. The coordinately unsaturated CoN_2 and FeN_2 sites were predominantly found in synthetic temperature above 900 °C whereas intact MN_4 configurations were observed at 800 °C.[90] This may be due to the loss of N at the extremely high temperature.

Effect of the ratio of metal precursors. If the mass ratio of target M atom to Zn atom (M:Zn) is controlled in a relatively low range, the pyrolyzed product, that exclusively contains atomically dispersed SAC sites (e.g., FeN_4), can be obtained via one-step pyrolysis without acid-leaching treatment[91, 92]. In some cases, an excessive M:Zn value is deliberately selected to produce metal aggregates near the SAC sites during pyrolysis, such as FeN_x and Fe/Fe_3C particles[93] or FeN_x and Fe_2O_3 particles.[19] These metal particles were found to improve ORR and HER performance[93-96]

by synergizing with the single metal active sites and by triggering the C−N bond cleavage during pyrolysis to form size-tunable mesopores in addition to edge-hosted FeN_4 sites (Figure 3a–b).[19]

Controlling the particle size of MOF precursors might be another strategy to tune the coordination environment of MN_4 sites for improved performance. Based on the dissociative mechanism, the edge-hosted MN_{2+2} sites (M = Fe, Co) were predicted to have higher ORR activity than in-plane MN_4 due to the lower dissociation barrier of OOH* on the MN_{2+2} site.[63, 97] Therefore, MOF precursors with smaller particle sizes tend to produce more MN_{2+2} sites after thermal activation, due to the higher ratio of edge area relative to the basal plane area. Our recent work showed that the particle sizes of Fe and Co SACs are tunable via controlling the size of the MOF precursors during the synthesis in solution. Both reducing the M/Zn ratio[92] and introducing high molecular weight surfactants[63] during MOF synthesis could downsize the particle size. The original morphologies, sizes, and abundance of MN_4 sites are retained in the final catalysts after thermal activation (Figure 3c–d). The surfactant layer coated on the Co-doped MOF precursor can form a carbon shell during pyrolysis that suppresses the agglomeration of Co atomic sites while simultaneously mitigating the collapse of internal microporous structures from the MOF precursor. Besides achieving higher active site density and better mass transfer, the highly active MN_{2+2} configuration appears to be predominant in the final catalyst, as evidenced by XANES and Mössbauer spectrum analysis.[63, 92]

Synthesis of dual metal sites from MOFs. Construction of Co-Fe dual-metal sites has been realized via a one-step pyrolysis of Fe-and Co- modified ZIF-8 MOF precursors (Figure 3e) in

which the Co atoms were chemically bonded to the nodes and the $FeCl_3$ molecules were encapsulated within cavities assisted by a double solvent method.[68] Different from isolated FeN_x and CoN_x sites, the EXAFS analysis suggests that the Fe-Co site had an unusual dual metal structure composed of two adjacent, Fe-Co bond linked FeN_3/CoN_3 configuration (Figure 3f). This method has been extended to synthesize Fe-Ni dual-metal sites.[76] In addition, Zn-Co dual-metal sites with a similar structure have been synthesized through a low-temperature pyrolysis, which leads to the incomplete volatilization of Zn atoms, followed by acid washing and a second thermal activation at 900 °C.[71] It should be noted that pyrolysis of dual-metal modified MOFs has also been used to synthesize electrocatalytically activate alloys on carbonaceous supports, such as Fe-Co, Fe-Mn and Fe-Ni alloy nanoparticles.[98, 99] Therefore, the ratio of metal precursors should be controlled to reduce the formation of metallic aggregates.

Synthesis of heteroatoms modified SACs. Pyrolyzing heteroatom-containing organic precursors is a common way to synthesize heteroatom (e.g., S, P and B) doped MN_x catalysts for electronic modulation of the active metal center via long-range interaction. Polymer or supramolecular composite precursors are usually more effective for forming stable carbonized substrates with high doping contents, while maintaining uniform distribution of dopant atoms, than small molecules due to their relatively high boiling points or decomposition temperatures. For example, Chen et al. reported the fabrication of isolated FeN_4 sites supported on N, P and S co-doped hollow carbon polyhedron from a S-, P-containing polymer coated MOF precursor (Figure 3g–h).[50] Besides acting as S and P resources, the polymer coating can lead to a hollow structure via the Kirkendall

effect. In addition, a S-doped FeN_x catalyst was prepared by pyrolysis of MOFs with $FeCl_3$ and NH_4SCN molecules encapsulated within the cavities through double solvent diffusion. During pyrolysis, gases released by NH_4SCN in the cavity interior lead to a hierarchical pore structure with an increased pore volume and surface area, resulting in improved ORR activity.[100]

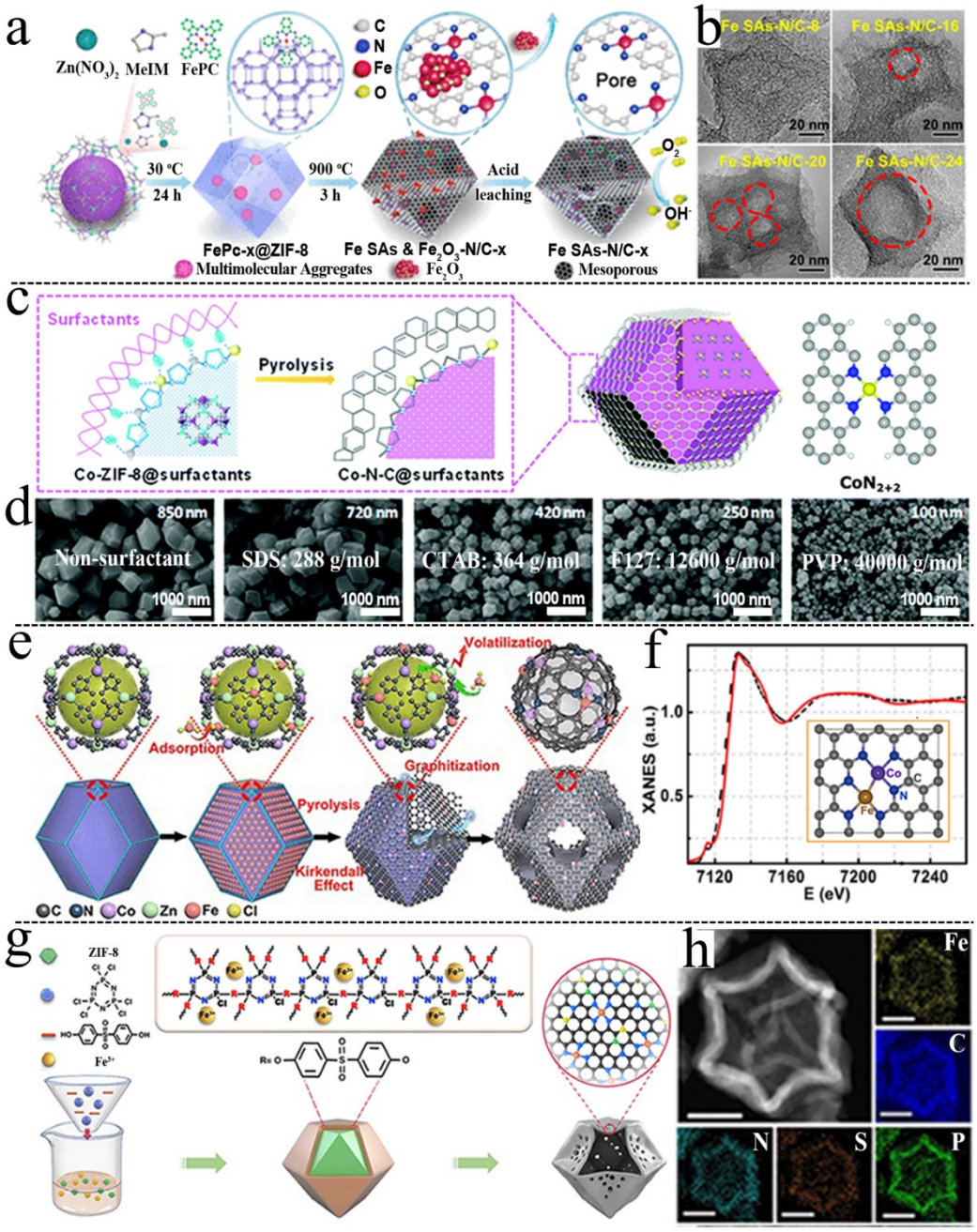

Figure 3. (a) Schematic illustration of the preparation of edge-hosted FeN_4 sites. (b) TEM images of FeN_4 SACs, showing the pore sizes is tunable by varying addition of Fe precursors. Reproduced with permission.[19] Copyright 2018, American Chemical Society. (c) Confinement pyrolysis strategy to synthesize Co SACs catalyst by using F127 surfactant. (d) SEM images of the catalysts

synthesized by using various surfactants, showing the variation in sizes and morphologies. Reproduced with permission.[63] Copyright 2018, The Royal Society of Chemistry. (e) Schematic illustration of the preparation of Co-Fe dual metal sites on N-doped porous carbon and (f) proposed molecular structure from XANEs analysis. Reproduced with permission.[68] Copyright 2018, American Chemical Society. (g) Schematic illustration of preparation of Fe SACs supported on N, P and S co-doped hollow carbon and (h) corresponding element mapping. Reproduced with permission.[50] Copyright 2018, Nature Publishing Group.

5.2 Trapping single metal sites by using vacancy

Different from pyrolysis methods, in which the SAC sites should be *in-situ* formed in one step, the vacancy trapping methods enable the formation of metal centers and corresponding coordination environments in separate steps. These types of methods demonstrate the possibility of designing the coordination environment on the substrate prior to the formation of SAC sites. In principle, diverse porous carbon materials with various doping elements and structures might be suitable substrates to anchor single metal atoms based on vacancy trapping methods. The defect and doping engineering of metal-free carbon materials for electron structural modulation has been extensively explored, providing an abundance of choices for carbon-based substrates and allowing for tuning of the electronic structure of the SAC. Vacancy trapping has been conducted under room or low temperature to ensure the structural integrity of the substrate during SAC fabriaction.

Vacancy trapping at high temperatures. Bulk Pt[101] or Cu[102] can be converted into volatile

$M(NH_3)_x$ species with the assistance of ammonia and can subsequently be captured by vacancies on the carbon-based substrate to form MN_xC_y moieties (Figure 4a-c). Some noble metal nanoparticles (Pd, Pt, Au-SAs) can be atomized above 900 °C in an inert atmosphere and converted into thermally stable single atoms, a phenomenon that has been observed by *in-situ* environmental transmission electron microscopy.[24]

Vacancy trapping at room temperature or low temperature. Different from harsh high-temperature pyrolysis procedures, several methods involve performing vacancy trapping of single atoms under room temperature conditions including ball milling, electrochemical methods, and impregnation-adsorption. High-energy ball milling of metal phthalocyanine and graphene oxide (GO) could produce the corresponding MN_4 centers (i.e., Mn, Fe, Co, Ni, and Cu) embedded into the graphene matrix, instead of forming phthalocyanine/graphene composites through π-π interactions.[103, 104] The mechanism involves the destruction of the outside macrocyclic structure to form residual MN_4 centers and sequential trapping of these MN_4 moieties by surface vacancies within the graphene. Graphdiyne supported Ni and Fe SACs have been prepared through adsorption of Ni and Fe ions and electrochemical reduction.[105] By controlling the electro-deposition time or potential cycle times during electrodeposition, atomic-level deposition of Pt on the counter electrodes can be achieved.[106] The dual-metal Co-Pt site on N-doped hollow graphitic spheres have been obtained by cyclic voltammetry, from 0.1 to 1.1 V vs. RHE, using CoN_x catalyst and Pt wire as the working and counter electrodes, respectively.[53]

Impregnation-adsorption is a simple and mild method to obtain carbonaceous substrate

supported SACs. This method only involves a liquid phase consisting of as-prepared N-doped carbon and metal ions at room temperature followed by a mild annealing treatment. For example, ultrathin N-doped graphene nanosheets from pyrolysis of g-C_3N_4 and glucose have been used to adsorb nickel nitrate in aqueous solution, followed by thermal annealing at 300 °C in Ar atmosphere to form isolated NiN_4 sites (Figure 4d).[107] Zhang et al. reported an adsorption-based synthesis of atomically dispersed Pt on N-doped or non-doped porous carbon and studied the formation mechanism through DFT calculations.[108] The results suggests that N-free micropores alone have the capability for trapping $[PtCl_6]^{2-}$ ions, but N atoms at the edge of micropores further strengthen the anchoring capability. The $[PtCl_6]^{2-}$ anions trapped in the micropores undergo de-chlorination at 70 °C to form N-coordinated Pt SACs. Also, a facile photochemical reduction method is effective to transform $[PtCl_6]^{2-}$ anions adsorbed in N-doped porous carbon into atomically dispersed and N-coordinated Pt SACs (Figure 4e).[109] The final samples exhibited high electrocatalytic performance without requiring any post treatment. In order to prevent uncontrolled nucleation and growth of metal particles at room temperature, a low temperature synthesis was also developed.[23, 110] Initially, a cobalt precursor underwent liquid-phase reduction with hydrazine hydrate at -60 °C to form an atomically dispersed Co species.[110] This first step is essential for facilitating the subsequent trapping of Co on N-doped porous carbon, which then undergoes heat treatment to form Co SACs. However, differing from the Pt-based sample that only needs mild thermal activation or photoreduction, the Co based sample seemed to require a higher annealing temperature (900 ºC) to form CoN_x sites and trigger catalytic activity.

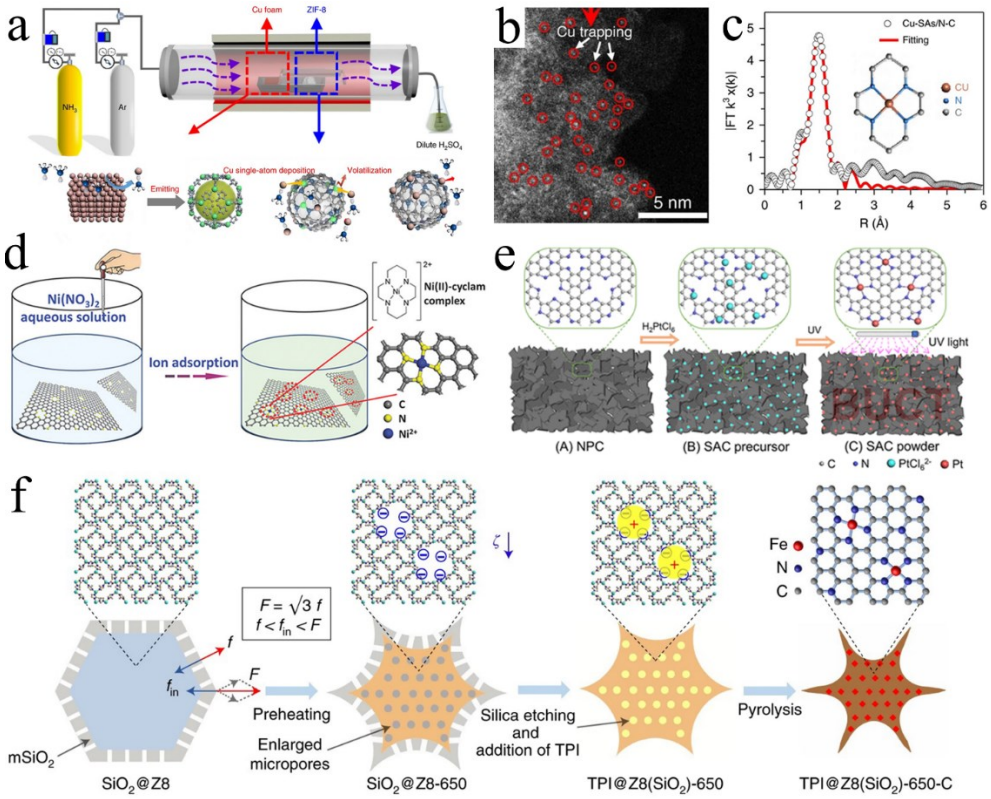

Figure 4. (a) Schematic illustration of the preparation of Cu SACs based on NH_3-assistant emitting and trapping of Cu atoms. (b–c) The HAADF-STEM image and EXAFS fitting curve of the Cu SACs. Reproduced with permission.[102] Copyright 2018, Nature Publishing Group. (d) Schematic illustration of Ni SACs based on an impregnation-adsorption method. Reproduced with permission.[107] Copyright 2018, Wiley-VCH. (e) Schematic illustration of the formation of Pt SACs through adsorption of $[PtCl_6]^{2-}$ and photoreduction. Reproduced with permission.[109] Copyright 2018, American Chemical Society. (f) Schematic illustration of silica template-assistant synthesis of mesoporous carbon supported FeN_4 sites by silica coating, preheating, etching silica off, absorbing Fe ions (TPI) and carbonization. Reproduced with permission.[111] Copyright 2019, Nature Publishing Group.

5.3 Template-assisted methods

In addition to the intrinsic activity and the density of SACs, mass transport properties are crucial for overall catalyst performance.[112] Different types of pores play different roles in MN_x based electrocatalysts. Micropores are highly related to the MN_x site density, [113, 114] mesopores promote electrolyte wetting of the catalyst surface to increase electrochemically available active sites,[115] and macropores facilitate kinetic accessibility of the active sites during the electrochemical reaction. Therefore, construction of SACs with hierarchical pore structures is highly desired for high-performance electrocatalysts. However, traditional pyrolysis processes tend to produce graphitized substrates with less-porous structures and metal particle aggregates. Direct formation of mesoporous structures with tunable porosity from traditional template-free precursors remains a grand challenge.

In order to maximize the density and utilization of the single-atom sites, many MN_x sites (e.g., Fe, Co, Ni, Mo, Cu) on porous carbon structures with various morphologies and pore size distributions have been developed using template-assisted methods. The types of templates can be divided into hard and soft templates. The studied hard templates include SiO_2 nanospheres,[111, 116-120] branched SiO_2 nanoaggregates,[121] ordered mesoporous SiO_2,[122] and MgO.[123] The soft templates involved Na_2CO_3,[124] KCl,[125] hydrogels,[85] and a self-assembled $FeCl_3$ layer.[126] For instance, Wan et al. reported the synthesis of atomically dispersed FeN_4 on concave-shaped octahedral carbon cages from SiO_2 coated ZIF-8 precursors.[111] The special processes include the silica coating, preheating, etching silica off, absorbing $[Fe(Phen)_3]^{2+}$ ions, and then carbonization

(Figure 4f). The unique concave morphology was created by the anisotropic thermal shrinkage of ZIF-8 with an external SiO_2 coating layer. The optimized sample exhibited excellent performance in proton exchange membrane fuel cells (PEMFC) application, attributed to the high active site density and efficient mass transport. Li et al. reported the synergistic utilization of $FeCl_3$ and SiO_2 templates to achieve porous carbon nanosheets with uniformly dispersed $FeCoN_x$ sites.[126] The $FeCl_3$ and SiO_2 served as the porogen and the hard template for micropore and mesopore formation, respectively.

6 Atomically dispersed single metal site electrocatalysis for energy conversion

6.1 Oxygen electrocatalysis for energy conversion

6.1.1 The oxygen reduction reaction

Precious metal-based SACs: The ORR is the limiting electrochemical process in many energy conversion devices. It could follow either four-electron ($4e^-$) or two-electron ($2e^-$) pathways, which are desirable for fuel cell cathodes and clean production of H_2O_2, respectively.[127] Pt-based alloy nanoparticles have been widely studied and commercialized for ORR applications.[5, 128-130] Differing from bulk Pt catalysts that mainly catalyze ORR in $4e^-$ pathways, the ORR mechanisms of Pt SACs were found to depend on the surrounding coordination atoms. The S-coordinated PtS_4 site[22] was experimentally determined to catalyze the ORR via the $2e^-$ reaction pathway, while N-[131] and C-coordinated[132] Pt single atoms prefer the $4e^-$ pathways. Besides the maximization of Pt utilization for enhanced mass activity, N coordination also endowed Pt atoms with unusual tolerance to carbon monoxide and methanol.[131] The C-coordinated Pt SACs for the ORR have

been synthesized using the vacancy trapping method under high temperature. The activity and stability of the C-coordinated Pt SACs were found to correlate strongly to the defect site density on the carbon substrate.[132] Using defect-free carbon black as substrate, the Pt SACs showed poor ORR activity and tended to aggregate into Pt nanoparticles. After being treated by H_2O_2, the defect-rich carbon black enabled the formation of atomically dispersed and stable Pt sites with promising ORR activity, presenting a half-wave potential ($E_{1/2}$) of 0.84 V in 0.1 M $HClO_4$ solution. DFT calculations revealed that the divacancy-anchored Pt configuration exhibits the lowest formation energy and has optimized adsorption energy for the rate-controlling OH* intermediates.

Non-precious metal-based SACs. Heteroatom coordinated MN_xC_y catalysts (M = Fe, Co, Cu, Mn ect.) are promising alternatives to Pt-based ORR catalysts.[133-135] The intrinsic activity of the atomically dispersed M active center highly depends on its local carbon structures, coordination environment and strain.[136] Modulating the electronic structure of SACs for enhanced ORR performance has been realized by several strategies, which are summarized in Table S1.

Synergy of SACs with heteroatoms. Heteroatom doping is an effective way to improve the ORR activity of carbon-based catalysts.[137, 138] Recently, synergistic effect between FeN_x sites and surrounding S heteroatoms have been demonstrated under both acidic and alkaline conditions. [29, 100, 122, 139, 140] However, the electronic modulation mechanisms remain controversial. The DFT calculations in many studies suggest that the reductive release of OH* ($*OH + 3OH^- + e^- \rightarrow 4OH^- + *$) should be the rate-limiting step if the ORR pathway follows the associative mechanism because the adsorption of OH* intermediates on the Fe center is too strong.[29, 50, 141] The expected

role of S doping is therefore to weaken the OH* binding which improves ORR activity and kinetics. In addition, XANES and XPS analyses revealed that the electron-donating thiophene-S is the main configuration in S, N co-doped carbon supported FeN_4. Due to the weaker electronegativity of S (2.58) compared to N (3.04), thiophene-S nearby the FeN_4 could induce a more negative charge on the N atom which is likely to repel the *OH, facilitating its desorption.[29] Chen et al. found that the P, S co-doping effect could change the charge density of the Fe center, improving the ORR activity of FeN_4 sites.[50] The Bader charge of the Fe center decreases linearly with the decrease in OH* binding energy in the order of FeN_4, P-doped FeN_4, and P, S co-doped FeN_4, resulting in gradually increasing ORR activity. Under 0.1 M KOH solution, the P, S co-doped FeN_4 exhibited an $E_{1/2}$ of 0.912 V with a Tafel slope of 36 mV dec^{-1}. Based on a similar synergistic mechanism, FeN_4 on B-doped carbon supports was also developed for improved ORR activity.[142] However, the opposite trend was observed for the effect of electronegativity on the activity of FeN_x sites. Recently, Mun et al. reported that the electron-withdrawing/donating properties of carbon substrates are indicative of Fe-N_4 ORR activity in acidic media, control of which was achieved by tuning the S doping (Figure 5a).[141] The XPS results revealed that a low S doping content on carbon substrates leads to predominantly oxidized S ($C–SO_x$) species with electron-withdrawing properties, while high S doping content provides more thiophene–S with electron-donating properties (Figure 5b). The introduction of $C–SO_x$ functionality could decrease the d-band center of Fe via the electron withdrawing effect, which lowers the adsorption energy of ORR intermediates on FeN_4, enhancing ORR activity (Figure 5c). The results above imply that other

factors, such as the location of doped atoms and the coordination state, may affect the structure-activity relationship of MN_x sites and should be further explored.

Similar to N-coordination, the coordinated O atoms also play a significant role in tuning the catalytic activity of the metal center. In addition, N-, O-coordinated Mn SACs have been synthesized and exhibit encouraging ORR performance in alkaline condition.[143] DFT calculations reveal that the improvement in activity of Mn atoms should be ascribed to the tuning of the local density of states (DOS) of the Mn d-orbitals via the change in the nearby electronic environment.

Effect of external ligands on activity of SACs. The electronic structure of the FeN_4 on S-doped carbon can be further optimized by introducing an external Cl coordination atom ($FeCl_1N_4$/CNS). The $FeCl_1N_4$ sites were fabricated by the addition of KCl and NaCl during pyrolysis of the porphyrin iron polymer, using SiO_2 as a hard template.[55] The EXAFS and Mössbauer spectra confirmed that the Fe in the $FeCl_1N_4$/CNS is coordinated by four N atoms and one Cl atom. DFT calculations revealed the Cl coordination broadens the d band of the Fe center, which may cause the d-band center shift down with respect to the Fermi level, weakening the binding energy of the ORR intermediates. The $FeCl_1N_4$/CNS exhibited excellent ORR performance with an $E_{1/2}$ of 0.921 V in 0.1 M KOH, outperforming most nonprecious metal electrocatalysts in alkaline media. In addition, pyrolysis of modified UiO-MOFs with bipyridine ligands as Fe anchor sites appears to produce an unconventional FeN_4 moiety coordinated with an external pyridine molecule (Fe-4pN-py). This also led to an optimized binding energy for *OH intermediates on the Fe center for better ORR activity.[81]

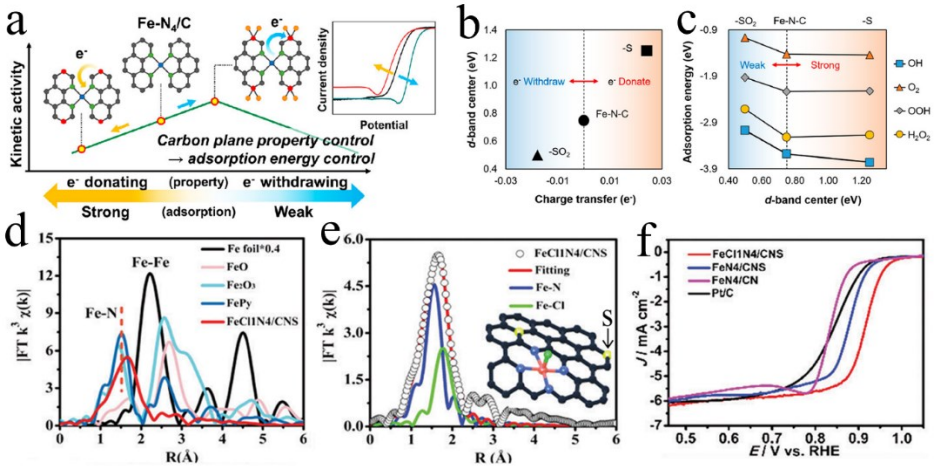

Figure 5. (a) The illustration of the electronic structural modification of FeN_4 moieties by using S doping and the corresponding trend of ORR activities. (b) The effect of charge transfer from the S-containing functional groups on d-band center. (c) The relationship between the adsorption energy of various intermediates and the d-band center. Reproduced with permission.[141] Copyright 2019, The American Chemical Society. (d−e) EXAFS spectra and (f) LSV curves of the $FeCl_1N_4$/CNS catalyst in 0.1 M NaOH. Reproduced with permission.[55] Copyright 2018, The Royal Society of Chemistry.

Possible synergy of SACs with metal particles. Although excessive metal agglomerations induced during pyrolysis are generally suggested to be electrochemically inert, and should be removed by acid washing, some metal species nearby the FeN_x sites were found to contribute to the enhanced ORR activity, including Fe/Fe_3C[93, 94] and Fe_4N particles.[96] The preparation of these electrocatalysts usually involves precise control of the precursor composition to form moderate amounts of metal particles. For example, the catalyst composed of FeN_4 sites and Fe/Fe_3C particles (1MIL/40ZIF-1000) was synthesized by pyrolysis of MIL-100(Fe) and a ZIF-8 mixture (Figure

6a–c).[93] The 1MIL/40ZIF-1000 without acid washing exhibited an improved ORR performance (Figure 6d–f), especially in 0.1 M KOH solution. The synergistic effects between Fe and Fe_3C were further investigated by DFT simulations. The free energy diagrams suggest that Fe_3C benefits the ORR by enhancing the O_2 affinity in the first O_2 adsorption step, and the metallic Fe promotes the rate-controlling *OH desorption from nearby FeN_4 sites (Figure 6j–i).

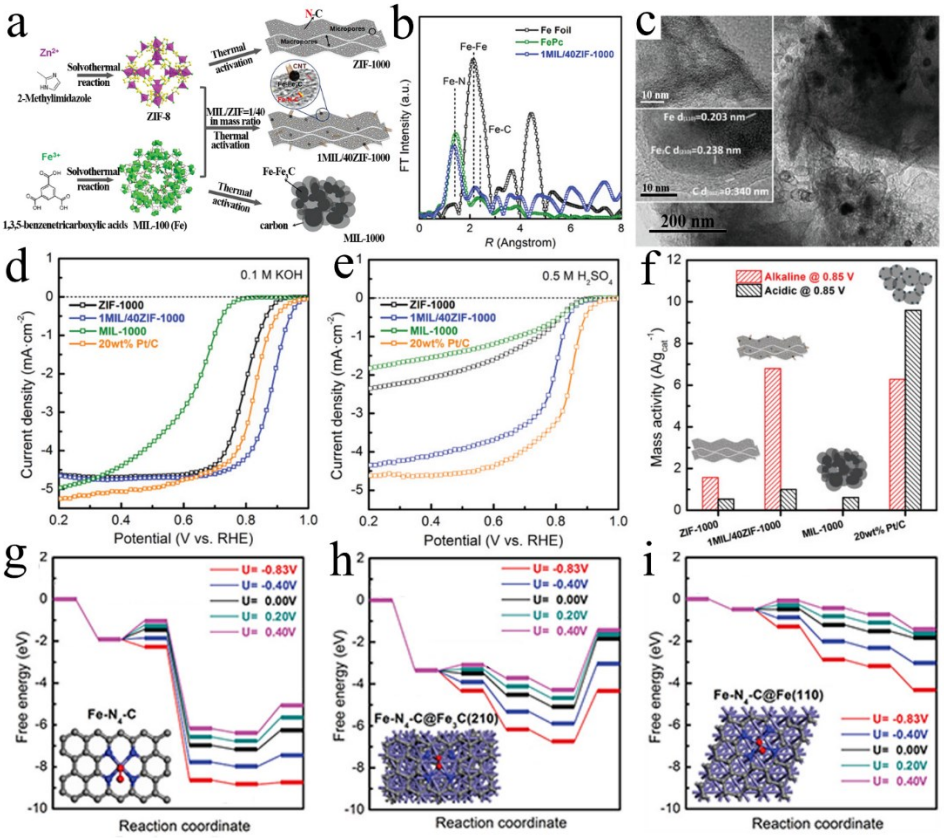

Figure 6. (a) Schematic illustration of the preparation of the ZIF-1000, 1MIL/40ZIF-1000, and MIL-1000 catalysts. (b) Fourier transforms of the experimental EXAFS spectra and (c) TEM image for 1MIL/40ZIF-1000, showing co-exist of Fe and FeC_3. (d-e) The LSV curves at 1600 rpm in 0.1 M KOH and in 0.5 M H_2SO_4, respectively. (f) Mass activity of the studied catalysts at 0.85 V. The ORR Free energy diagram for (j) Fe–N_4–C, (h) Fe–N_4–C@Fe_3C (210), and (i) Fe–N_4–C@Fe (110) in alkaline media. Reproduced with

permission.[93] Copyright 2019, Wiley-VCH.

Edge and defect engineering. The ORR activity of FeN_4 sites can also be improved by edge and defect engineering. Jiang et al.[19] synthesized edge-hosted FeN_4 sites, with the assistance of Fe_2O_3 particles, that exhibited a high $E_{1/2}$ of 0.915 V in 0.1 M KOH. Using NH_4Cl as a porogen, Fu et al.[64] synthesized an edge- and pore-enriched FeN_4 catalyst that showed encouraging ORR activity in 0.5 M H_2SO_4. DFT caculations reveal that edge and pore defects play a key role in modulating the electronic structure of adjacent FeN_4 sites, leading to an optimized adsorption energy of the intermedates and a remarkably decreased ORR barrier compared to the nondefective configuration.[97]

Synergism of dual metal sites. The construction of dual metal sites has been demonstrated to be highly effective for enhanced ORR performance. A series of N-coordinated dual metal sites, including Co-Fe,[67-70] Co-Pt,[53] Zn-Co[71, 72] and Fe-Mn[73] sites, have been developed. Their ORR activities are usually higher than the corresponding single metal sites. For example, the bi-metallic Co-Fe sample synthesized by Zhang et al. exhibited outstanding ORR performance in both alkaline and acidic medias.[69] In addition, the $E_{1/2}$ of the bi-metallic Co-Pt sample reached a high value of 0.96V, significantly higher than that of Pt/C.[53] The enhancement mechanisms were investigated by DFT caculations and it was found that the charge redistribution between different metal centers could modulate the local electronic structure, thus improving the intrinsic ORR activity. The specific structure simultaneously provides two active adsorption sites, which may change the

adsorption behavior of the reactants and intermediates, thus providing an optimized reaction pathway with a lower energy barrier.[67, 68, 71] Liu et al. further combined dual metal sites and S-doping to improve ORR activity.[72] They synthesized Zn-Co dual sites on a N, S co-doped carbon support, (Zn, Co)/NSC, through pyrolysis of chitosan, urea, sodium diethyldithiocarbamate, $Co(acac)_2$, and $ZnCl_2$, followed by acid washing and a second annealing treatment. The unique Zn-Co bimetallic structure could reduce the dissociation barrier of *OOH into *O and OH^- by elongating the O–O bond length. As a result, all reaction steps become downhill in free energy under applied potentials below 0 V for (Zn, Co)/NSC. Using S doping to modulate the charges around the Zn-Co active center further optimizes the adsorption energy of O-containing intermediates in the ORR process. The (Zn, Co)/NSC sample exhibited high catalytic activity with an $E_{1/2}$ of 0.89 V in 0.1 M KOH.

SACs ORR for PEMFCs. For alkaline ORR, evaluated by the rotating disk electrode (RDE) test, many MN_x based electrocatalysts have exhibited superior activity to commercial Pt/C.[144-146] However, achieving comparable ORR performance to commercial Pt/C under acidic conditions, especially in the practical application of proton exchange membrane fuel cells (PEMFC), is a grand challenge.[147, 148] Among PGM-free electrocatalysts, Fe based MN_x materials have demonstrated the highest activity in PEMFCs.[149] The parameter optimizations, which include intrinsic activity,[64, 68] active site denstiy,[91, 111] mass transport property[150, 151] and conductivity,[152] have been performed on FeN_x by several research groups to improve the performance in membrane electrode assemblies (MEAs). For instance, the introduction of highly electrical conductive CNTs

(carbon nanotubes) could network the carbonaceous support with FeN_x sites for improved electron/proton conductivity.[152-154] A template-assisted synthesis with SiO_2 increased both the FeN_4 site density and the mass transfer by improving the external surface area and mesoporosity. The optimized catalyst reached the U.S. DOE activity target for PEMFC performance as well as a current density of 129 mA cm^{-2} at 0.8 $V_{iR\text{-}free}$ under a 1.0 bar H_2–air atmosphere. Using Fe-modified ZIF-8 as precursor, the effects of Fe/Zn ratio, heating tempurature, and particle size on the performance in MEAs were systematically studied by Wu and co-workers.[60, 92] They showed that the Fe:(Zn+Fe) molar ratio of 1.5% in ZIF-8 precursor and 1100 ºC are the optimal preparation conditions, which give rise to high FeN_4 site density, without Fe particles, and results in a suitable graphitization degree as well as relatively small particle size (Figure 7a). The Mössbauer spectra indicated that the edge-hosted FeN_{2+2} sites (D1), which have higher intrinsic activity than the bulk-hosted FeN_4, were predominant in the obtained catalyst (Figure 7b). This catalyst also exhibited encouraging activity in MEA tests, with a current density of 0.044 A cm^{-2} at 0.87 $V_{iR\text{-}free}$ under a 1.0 bar H_2–O_2 atmosphere and a peak power density of 360 mW cm^{-2} under a practical 1.0 bar H_2–air atmosphere (Figure 7c–e).

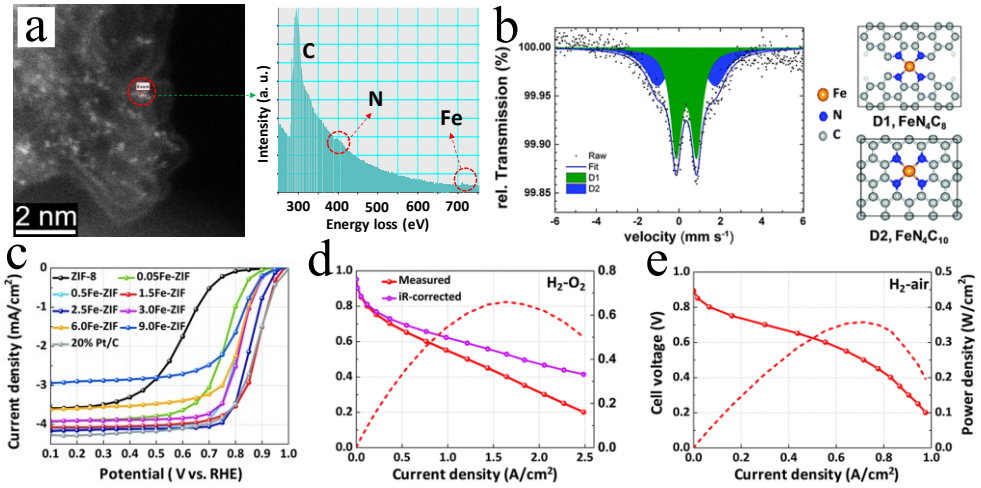

Figure 7. (a) Experimental observation of atomically dispersed FeN_x by HAADF-STEM image coupled with EELS. (b) Mössbauer spectra of the best performing atomically dispersed Fe catalyst, showing two main Fe configuration: the D1 (FeN_4C_8) and D2 (FeN_4C_{10}). (c) LSV curves for different FeN_4 catalysts obtained from precursors with different Fe content. (d–e) Polarization curves and power density of optimum FeN_4 catalyst under 1.0 bar H_2–O_2 and H_2–air conditions, respectively. Reproduced with permission.[92] Copyright 2019, The Royal Society of Chemistry.

Despite having high activity, FeN_x catalysts can catalyze the undesirable Fenton side reaction to generate free radicals, which causes carbon corrosion and active site loss. Thus, atomically dispersed Co[155] or Mn[134, 156] catalysts, which have relatively low catalytic activity for the Fenton reaction, have been developed for application in acidic ORR and realistic PEMFC application. Similar to FeN_x, pyrolysis of Co or Mn modified MOFs is an effective method for the synthesis of CoN_x and MnN_x catalysts. For CoN_x, the synthetic conditions, such as the Co/Zn ratio or pyrolytic temperature, were found to affect the N-coordination of the final products. Coordinately

unsaturated CoN_2 sites,[88] edge-hosted CoN_{2+2} sites[63] and binuclear Co_2N_5 sites[157] have been identified to exhibit superior ORR activity to that of the intact CoN_4 configuration, attributed to the change in the local electronic environment of the Co atom that results in optimized adsorption/desorption strengths of the ORR intermediates. In particular, atomically dispersed Co sites with high atomic density (Co–N–C@F127) have been synthesized by direct pyrolysis of Co and F127 surfactant modified ZIF-8 MOFs at 900°C.[63] The Co–N–C@F127 catalyst exhibited an unprecedented ORR activity among Co based SACs, with an $E_{1/2}$ of 0.84 V, as well as good stability in 0.5 M H_2SO_4 solution. DFT calculations predicted that the edge-hosted CoN_{2+2} sites are able to catalyze the ORR via $4e^-$ pathways more effectively than CoN_4 sites and are responsible for the increased activity over Fe-based catalysts. Furthermore, the Co–N–C@F127 also demonstrated considerable PEMFC performance with a power density of 0.87 W cm^{-2} under a 1.0 bar H_2–O_2 atmosphere. In another work, Li et al reported a dual metal Fe-Co catalyst ((Fe-Co)/NC) derived from an Fe, Co co-modified MOF precursor, which showed a high $E_{1/2}$ of 0.863 V in acidic media.[68] Importantly, the (Fe-Co)/NC exhibited good activity and stability when applied in the PEMFC cathode, with negligible working voltage loss after 100 h of constant-current operation tests under H_2/air working conditions.

6.1.2 The oxygen evolution reaction

The OER, which is the reverse reaction of the ORR, is essential for water splitting and rechargeable metal–air batteries. MN_x (M = Ni, Co, Fe, and Mn) sites have proven to be effective OER electrocatalysts.[158, 159] To comprehensively describe the electrocatalytic activity of MN_x based

materials for the OER, recent works are summarized in Table S2.

OER activity of different metal center: Several MN_4C_4 sites have been synthesized with different metal centers and exhibited the OER activity trend of Ni > Co > Fe.[20] The identical MN_4C_4 configuration for these catalysts was unambiguously confirmed by the XANES analysis and direct TEM imaging (Figure 8a–d). DFT calculations (Figure 8e–g) and OER tests (Figure 8h) revealed that different metal active centers lead to different OER mechanisms and catalytic activity which is attributed to the adsorption energy differences toward the intermediates (O*, OH* and OOH*) between the metal centers and surrounding C atoms. As all intermediates are more readily adsorbed on the metal center than other possible active sites, the OER is suggested to follow the single site mechanism for FeN_4C_4 and CoN_4C_4 (Figure 8e). For the NiN_4C_4 site, both Ni and C atoms were involved in the reaction because O* and OH* adsorb stronger onto C atoms whereas OOH* adsorbs stronger onto Ni atoms, leading to an optimized reaction pathway via the dual-site mechanism for enhanced OER activity (Figure 8f–g). To further improve the OER performance of Ni based SACs, coordinated-S atoms have been introduced to modify local electronic structures. Hou et al. reported atomically dispersed Ni atoms on N and S co-doped porous carbon supports ($S|NiN_x$-PC/EG) (Figure 8i).[54] According to the calculated formation energy and OER overpotentials for different models, the NiN_3S configuration was predicted to be the best active site. The $S|NiN_x$-PC/EG showed enhanced OER performance compared to the S-free control with an overpotential of 280 mV at 10 mA cm^{-2} and a Tafel slope of 45 mV dec^{-1} in alkaline media (Figure 8j). Because S atoms are less electronegative than N atoms, the coordinated S atoms could

reduce the electron donation of the Ni atom to its neighboring N atoms (Figure 8k), thereby optimizing the hybridization states between Ni and the neighboring N atoms, and resulting in enhanced OER activity. Likewise, MnN_4 sites embedded in a graphene plane (Mn-NG) have been studied, showing an overpotential of 337 mV at a current density of 10 mA cm^{-2} in alkaline media.[160] The Tafel slope of Mn-NG (55 mV dec^{-1}), which is close to precious metal catalysts, is far smaller than that of the N-free control sample (139 mV dec^{-1}), indicating faster reaction kinetics. The reaction mechanism was further studied by DFT calculations. The increased activity of MnN_4 over other Mn-based species was ascribed to a more efficient reaction pathway. The MnN_4 site first facilitates the formation of Mn–O intermediates which can act as new active sites to activate H_2O molecules, leading to Mn-OOH intermediates that can release O_2 over a lower energy barrier.

In addition to N-coordinated SACs, theoretical predictions revealed promising OER activity for C-coordinated NiC_4 sites compared to other nonprecious metal SACs (e.g., Ni, Mn, Fe, Co, Cu, and Mo).[37] The OER activity for NiC_4 based SACs has also been experimentally demonstrated by Zhang et al., showing a reduced overpotential of 270 mV at 10 mA cm^{-2} and a Tafel slope of 47 mV dec^{-1} in 1.0 M KOH solution.[18]

SACs on crystalline g-C_3N_4. Different from amorphous N-doped porous carbon, crystalline g-C_3N_4 has a long-range ordered structure and dense N coordination sites which are ideal for anchoring metal atoms and modifying their electronic structures. This also facilities to accurately define local coordination environments of SACs and simulate reaction mechanisms. According to DFT

predictions, the Co atom anchored on g-C_3N_4 shows the best OER activity amongst g-C_3N_4 supported SACs (e.g., Pt, Pd, Ni, and Cu).[161] However, from a practical electrocatalytic application point of view, the electrical conductivity of g-C_3N_4 based SACs needs to be improved. Highly conductive CNTs were utilized as carbonaceous skeletons to prepare Co SACs on a g-C_3N_4 matrix through one-step pyrolysis of Co salt, dicyandiamide, and CNTs at 600 °C.[162] DFT calculations predicted that the Co atom might be stabilized by two adjacent pyridine-N atoms, from two separate triazine units, due to the lowest formation energy, which is consistent with EXAFS results. The optimized catalyst showed an overpotential of 337 mV at 10 mA cm^{-2} and a Tafel slope of 73.9 mV dec^{-1} in 1.0 M KOH. Moreover, obvious decline in OER activity was observed for the control sample after carbonization treatment at 900 °C due to the decomposition of g-C_3N_4, indicating the key role of g-C_3N_4 in modulating the electronic structure of the Co atom.

Synergism of dual metal sites. Using an identical synthetic strategy, atomically dispersed Ni and Fe SACs on g-C_3N_4/CTNs were obtained that experimentally demonstrated a synergistic effect of Ni-Fe dual metal sites on g-C_3N_4.[163] The OER kinetics were further analyzed by examining Tafel plots. In another work, the mechanism of active enhancement for Ni-Fe sites was further discussed.[164] The Ni-Fe dual metal sites exhibited a smaller Tafel slope (38 mV dec^{-1}) and a lower overpotential (310 mV at 10 mA cm^{-2}) when compared to single metal Ni or Fe sites. DFT calculations suggest that the adjacent Ni-Fe atoms simultaneously provide two different adsorption sites for reactants and intermediates leading to an optimized reaction pathway with a lower overall activation energy barrier. Compared to dual metal sites, the electronic modulation of the single

metal site (either Fe or Ni) induced by the interaction between two metal atoms contributes less to the activity enhancement. It should be noted that, in addition to intrinsic activity, catalyst stability in the challenging OER environment is always a serious concern. Most amorphous carbon components in catalysts suffer corrosion at a potential beyond 1.0 V.[165] Therefore, implementing carbon-based SACs for the OER still remains a grand challenge.[160]

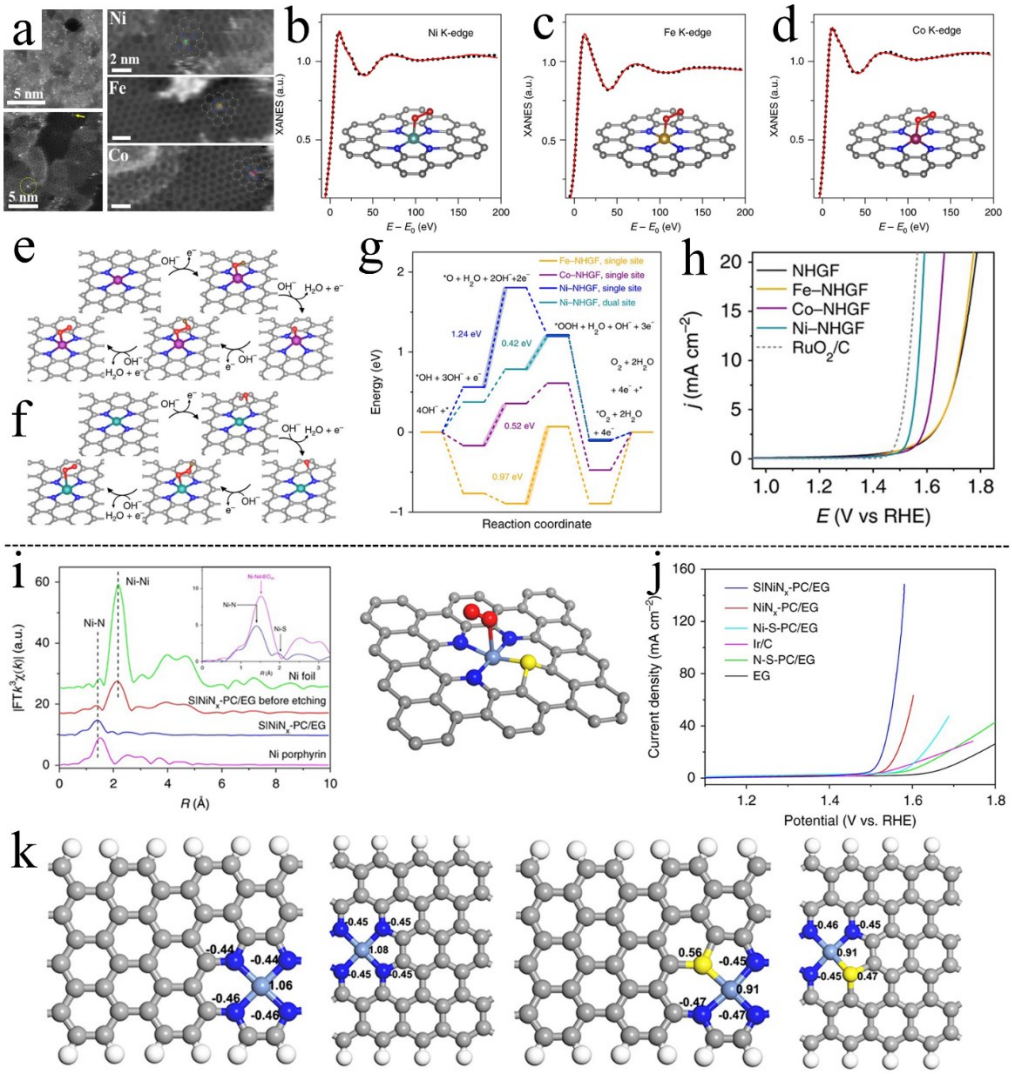

Figure 8. (a) TEM imaging and (b–d) XANES spectra with fit theoretical spectra for MN_4C_4. The suggested OER mechanisms for Co or Fe based MN_4C_4 (e) as well as for NiN_4C_4 sites (f). (g) Free energy diagram of OER on different MN_4C_4 sites. (h) OER LSV curves of MN_4C_4 in 1.0 M KOH solution. Reproduced with permission.[20] Copyright 2018, Nature Publishing Group. (i) Ni K-edge EXAFS spectra and possible molecular structure of the S- doped Ni SACs. (j) OER LSV curves of S-doped Ni SACs and corresponding controls. (k) Population distributions for the DFT-calculated NiN_3S models (light blue: Ni; dark blue: N; yellow: S; gray: C). Reproduced with permission.[54] Copyright 2019, Nature Publishing Group.

6.1.3 Bifunctional ORR/OER

Some N-coordinated SACs, which have demonstrated their bifunctional ORR/OER activities, can serve as effective electrocatalysts for reversible alkaline fuel cells and rechargeable metal-air batteries. Several CoN_x,[166, 167] FeN_x,[168-170] B-doped CoN_x[171], S-doped FeN_x[172] and Co-FeN_x[126] based bifunctional SACs supported on N-doped porous carbon have been developed and studied for bifunctional ORR/OER applications in fuel cells and batteries. For example, uniformly dispersed CoN_4 sites with a Co loading of ~15.3 wt.% has been achieved by pyrolysis of KCl wrapped ZIF-67 MOFs.[125] In 0.1 M KOH solution, it showed excellent electrocatalytic performance with a $E_{1/2}$ of 0.91 V for ORR and overpotential of 310 mV at a current density of 10.0 mA cm^{-1} (Figure 9a–b). A rechargeable Zn-air battery with the bifunctional electrocatalyst exhibited a peak power density of 150 mW cm^{-2}, a specific capacity of ~690 mAh g_{Zn}^{-1} at a current density of 5 mA cm^{-2} (corresponding to an energy density of 945 Wh kg_{Zn}^{-1}), and excellent cycle stability (Figure 9c–f).

Similar to ORR or OER, multiple heteroatom-doping and construction of dual metal sites has been demonstrated to be an effective tactic for enhancing the bifunctional ORR/OER performance of MN_x sites. B-doping was found to simultaneously promote ORR and OER activities of CoN_x based catalysts,[171] but the involved mechanism remains elusive due to complexities related to the possible activity of B-doped C sites. Improving the ORR/OER activity of FeN_x by S-doping has also been reported, where S-doping simultaneously improved both the ORR and OER activity.[172]

The CN^- treated catalyst showed an obvious decrease in OER activity, indicating the predominant role of S-doped FeN_x sites for the OER. In another work, the introduction of Fe atoms was found to enhance the ORR/OER performance of the CoN_x based catalyst, but the specific mechanism was not discussed.[126]

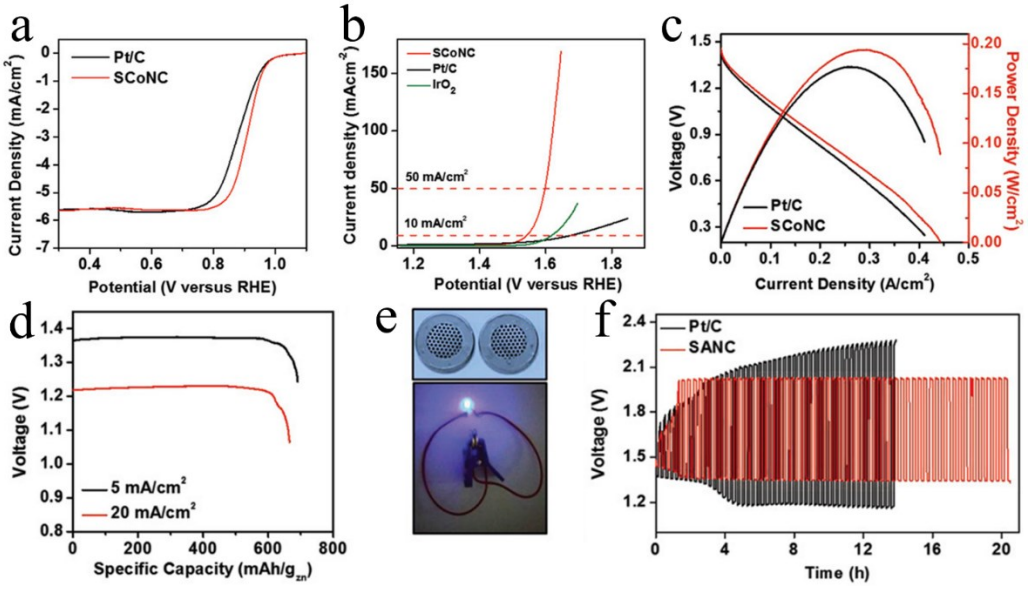

Figure 9. Polarization curves of Co SACs for (a) ORR and (b) OER at 1600 rpm in 0.1 M KOH. (c) Discharge curves and corresponding power density curves of Zn-air batteries based on Co SACs. (d) Discharge tests of Co SACs oxygen electrode in a Zn-air battery until the Zn electrode was completely consumed. (e) A 2.5 V LED driven by two Zn-air button cells in series. (f) Discharge/charge cycling curves of Zn-air batteries at 5 mA cm^{-2}. Reproduced with permission.[125]

6.2 The hydrogen evolution reaction

Water splitting based on electrochemical HER ($2H_2O + 2e^- \rightarrow H_2 + 2OH^-$), coupled with

renewable electricity sources, is an option for mitigating the energy crisis. Many noble and non-noble metal-based SACs have been used to catalyze the HER. To gain further insight into the effect of local atomic environments on HER performance, SACs with different configurations are summarized in Table S3.

Noble metal-based SACs. As discussed in section 2, ΔG_{H^*} is widely used as a descriptor for HER activity. According to the volcano plots, Pt should be the best HER catalyst in acidic media due to the nearly zero ΔG_{H^*}. Generally, the HER activity of commercial Pt/C catalysts is limited by the desorption of H* because the value of ΔG_{H^*} is slightly below zero.[101] Therefore, the role of coordination is to weaken the H* binding energy while improving atomic utilization. Since Pt is highly stable in both acids and bases, it is difficult to isolate single Pt atoms by removing Pt clusters and nanoparticles through traditional acid-leaching methods. Thus, several vacancy trapping methods have been developed to prepare atomically dispersed PtC_x[101] and PtN_x[108, 109, 173] sites, which exhibit lower overpotentials, a smaller Tafel slope, and offer considerably higher stability compared to that of the commercial Pt/C catalyst. The enhanced performance of Pt SACs compared to bulk Pt results from the charge transfer from Pt to adjacent C/N atoms, as reflected in the higher oxidation state of Pt in XANES and the Bader charge analysis, which leads to the change of unoccupied d orbitals of single Pt atoms, favoring the HER process.[174] Interestingly, HER free energy diagrams of PtN_x sites reveal that the binding strength of H* is weakened with an increase in H coverage of the Pt atom surface.[173] Thus, simultaneously binding two or more H atoms on a single Pt atom to catalyze the HER process follows the Tafel mechanism.

While Pt-based SACs have demonstrated excellent HER activity in acidic media, the HER kinetics of Pt catalysts in alternative alkaline media are still far from satisfactory due to the high energy barrier of the initial water molecule dissociation, a unique step that is unseen during the HER in acid.[175, 176] To this end, Ru-based SACs were explored and found to exhibit high HER activity in alkaline media.[177, 178] Experimental results and DFT calculations suggest that atomically dispersed RuC_2N_2 moieties, which have a lower kinetic barrier for water dissociation than Pt, are most likely the active sites of highest activity, while the contributions from Ru nanoparticles are minimal. The optimized catalyst performs better than the Pt/C catalyst, with an overpotential of 12 mV in 1.0 M KOH and 47 mV in 0.1 M KOH at 10 mA cm^{-2}.

Effect of extra ligand and location on activity of SACs. Engineering the local atomic environment of single Pt atoms for the HER has been reported by several works, strategies include tuning the coordination atoms[83] and changing the location of Pt atoms.[47] The graphdiyne supported Pt atoms with four external Cl ligands (Pt-GDY1) were synthesized by impregnating the as-prepared graphdiyne in K_2PtCl_4 aqueous solution at 0 °C for 8h.[83] After an annealing treatment at 200 °C, the Pt-GDY1 could be further transformed into low-coordinated Pt-GDY2 moieties with two Cl ligands (Figure 10a). The electronic structure and coordination environments of these two samples were confirmed by XAS analysis. Reducing the Cl coordination number weakens the H* adsorption, leading to an optimized ΔG_{H^*} for the Pt-GDY2 sample and an enhanced HER performance over both Pt-GDY1 and Pt/C (Figure 10b–c). Although Pt-GDY1 has a more negative ΔG_{H^*} than commercial Pt/C, it still exhibited a higher mass activity due to its superior Pt utilization.

Liu et al. reported the synthesis of Pt SACs on highly curved carbon nanospheres (Pt_1/OLC).[47] The surface-oxidized detonation nanodiamonds were first treated by thermal annealing at 1500°C to form an onion-like carbon nanospheres (OLC) with a suitable type and distribution density of oxygen species for anchoring Pt atoms. The atomic layer deposition (ALD) method was used to produce isolated Pt atoms on OLC supports stabilized by one carbon atom and two oxygen atoms. The Pt_1/OLC catalyst exhibited greater HER activity than the 2D graphene supported Pt atom control, attributed to the unique spherical support that enabled the formation of tip-like Pt sites (Figure 2b). DFT calculations revealed that the tip-enhancement effect could trigger electron accumulation around the Pt sites, inducing strong localized electric fields that increase the H^+ coverage on Pt atoms, thus enhancing HER kinetics.

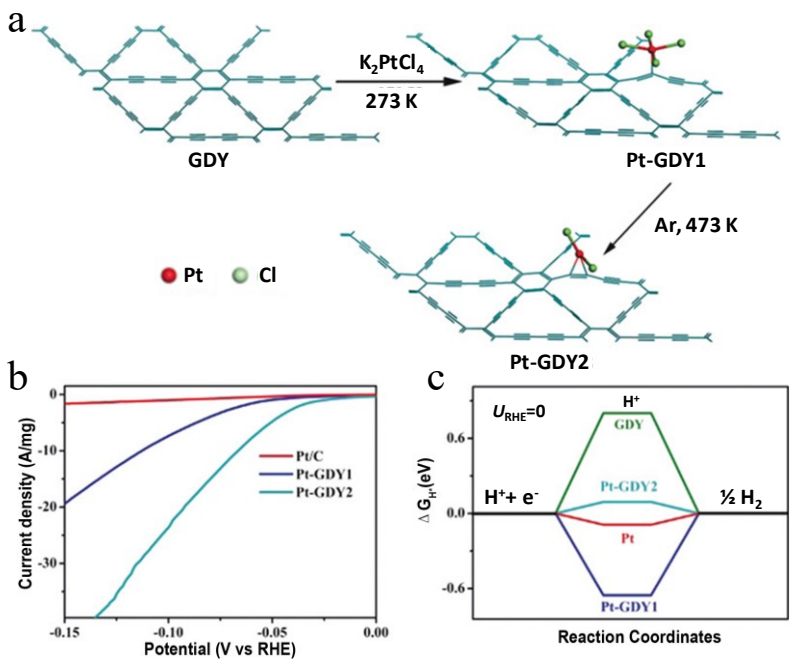

Figure 10. (a) Schematic illustration of the preparation of graphdiyne supported Pt atoms with four Cl ligands (Pt-GDY1) and with two Cl ligands (Pt-GDY2). (b) The LSV curves for Pt-GDY1, Pt-GDY2, and commercial Pt/C in 0.5 m H_2SO_4 solution. (c) The calculated ΔG_{H^*} for GDY, Pt-GDY1, Pt-GDY2, and bulk Pt control. Reproduced with permission.[83] Copyright 2018, Wiley-VCH.

Non-noble metal-based SACs: Many non-noble metal-based SACs have also been synthesized that exhibited good HER activities, including NiN_x,[95] CoN_x,[46, 117, 179-182] NiC_x,[17, 18] and graphdiyne supported Fe^0/Ni^0 in acidic media, [105] and both MoN_1C_2[118] and WN_1C_3[183] in alkaline media. The enhanced intrinsic activity should be ascribed to the unique coordination environment of the metal centers.[184] For example, MoN_1C_2 [118]and WN_1C_3[183] exhibited comparable performance to the Pt/C benchmark in 1.0 M KOH. DFT calculations predicted that the unique coordination structures could lead to higher density of states (DOS) near the Fermi level for W and Mo based SACs, thus optimizing the ΔG_{H^*}. The WN_1C_3 exhibited an overpotential of 85 mV at 10 mA cm^{-2}, a Tafel slope of 53 mV dec^{-1}, and a TOF value of 6.35 s^{-1} at 120 mV with negligible activity change after 10000 CV cycles in 0.1 M KOH solution. Cao et al. synthesized atomically dispersed Co atoms anchored onto a P-doped g-C_3N_4 support (Co_1/PCN) and studied the HER process using operando XAS technology.[182] The Co atom stabilized by two adjacent pyridine-N atoms were found to further bond with one OH^- group to form a HO–Co_1–N_2 configuration that was suggested to be the real active site for the HER. The OH^- ligand, with its strong electronegativity, further increases the oxidation state of the Co center, reducing the energy barrier of the H_2O dissociation

step.

Synergy of SACs with metal particles. The possible synergistic effects between NiN_4 sites and Ni particles in alkaline media have been studied (Figure 11).[95] The presence of Ni nanoparticles was found to optimize the surface states of NiN_4 active centers and reduce the energy barrier of dissociating H_2O molecules (Figure 11d–e), synergistically promoting HER kinetics. The overpotential of optimized samples (Ni NP|Ni-N-C/EG) exhibited an overpotential of 147 mV at 10 mA cm^{-2} with considerable stability (Figure 11a–c). The Tafel slope of the Ni NP|Ni-N-C/EG was -114 mV dec^{-1}, much higher than that of the control sample without Ni particles (-183 mV dec^{-1}). This result indicates that Ni NP|Ni-N-C/EG follows a more efficient Volmer–Heyrovsky mechanism,[185] and the slow Volmer step is significantly accelerated by introduction of Ni particles.

Synergy of dual metal sites: Construction of dual-metal sites is a promising way to modify the local electronic structure of SACs. A Co-Pt dual-metal site on hollow multilayered carbon shells (A-CoPt-NC) was synthesized by pyrolysis of Co-based MOFs followed by electrodeposition of Pt atoms.[74] The STEM images and XAS spectra indicate that the Co-Pt sites were stabilized by eight N atoms and four C atoms to form two adjacent pyridine-type MN_4 configurations. The A-CoPt-NC exhibited high HER activity in both acidic and alkaline media, with overpotentials of 27 mV in 0.5 M H_2SO_4 and 50 mV in 1.0 M KOH at 10 mA cm^{-2} (Figure 11i–g). In addition, the HAADF-STEM images of A-CoPt-NC after fast Fourier transformation revealed that these Co-Pt sites were trapped in 3D graphitic layers, including the outermost and inner layers (Figure 11f–h). DFT calculations revealed that the inner Co-Pt sites could induce a new charge redistribution on

the outermost Co-Pt sites, which eliminates the charge depletion on the outermost Co atoms, leading to stronger adsorption of H^+ and improved HER activity (Figure 11k–m). This theoretical prediction was experimentally verified by the superior activity of Co-Pt sites on multilayer layer graphene relative to single layer graphene (Figure 11n).

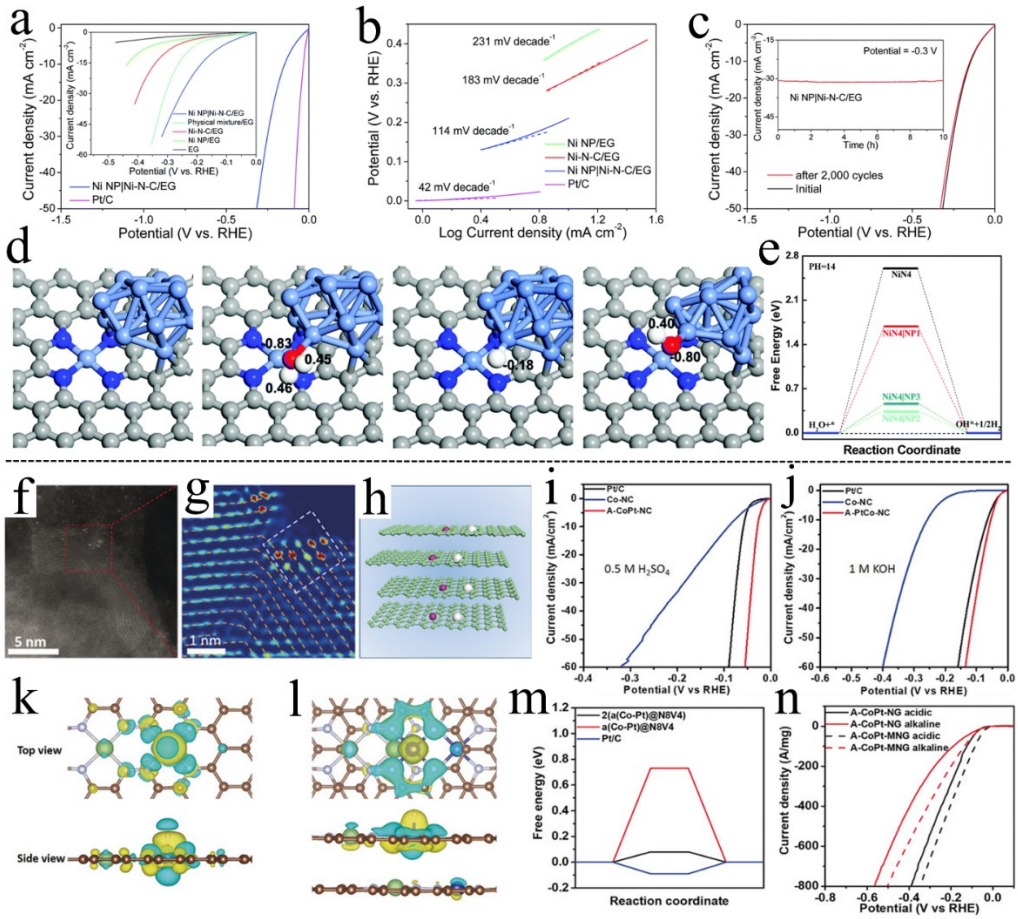

Figure 11. (a) LSV curves and (b) Tafel plots of Ni NP|Ni-N-C/EG and control samples for the HER in 1.0 M KOH solution. (c) HER LSV curves of NP|Ni-N-C/EG before and after 2000 cycles. (d) DFT calculated models and corresponding population distributions of the groups adsorbed for NiN_4 sites with adjacent Ni

particle. The gray, light blue, blue, red and white represent the C, N, Ni, O and H atoms, respectively. Reproduced with permission.[95] Copyright 2019, The Royal Society of Chemistry. (f) The HAADF-STEM image of A-CoPt-NC and (g) corresponding image after fast Fourier transformation (FFT) filtering. (h) Illustration of the 3D structure of A-CoPt-NC. The pink and white represent the Co and Pt atoms. (i–j) LSV curves of A-CoPt-NC and control samples in 0.5 M H_2SO_4 and 1.0 M KOH. (k–l) Side view and top view of the charge distribution of single/double layered model of Co-Pt sites. The brown, white, green and blue represent the C, N, Pt and Co atoms, respectively. Yellow and cyan represents electron accumulation and depletion, respectively. (m) Free energy profile and (n) LSV for both A-CoPt-NG and A-CoPt-MNG catalysts in both acidic and alkaline solutions. Reproduced with permission.[74] Copyright 2019, Wiley-VCH.

6.3 CO_2 reduction reactions

Electrochemical CO_2RR under ambient conditions represents a promising approach to mitigate CO_2 emissions while generating value-added fuels and chemicals.[186] Non-noble metal based MNx catalysts that have demonstrated impressive activity for the electrochemical reduction of CO_2 to CO are summarized in Table S4. The CO_2RR process on MN_x usually involves the follow three steps:

$$CO_2 + HA + e^- + * \rightarrow *COOH + A^- \quad (6)$$

$$*COOH + HA + e^- \rightarrow *CO + H_2O + A^- \quad (7)$$

$$*CO \rightarrow CO + * \quad (8)$$

where HA represents a general acid proton donor (*e.g.*, H_2O, H_3O^+, HCO_3^-, H_2CO_3) and A^- is its conjugate base.

CO_2RR activity of different metal center: Both the nature of the metal site and the corresponding coordination environment can affect the adsorption energies of *COOH, *CO, and CO on MN_4, thus determining their activity and selectivity during the CO_2RR. The combination of theory and experimental results suggests that the CO_2RR activity of MN_4 sites follows the trend Ni ≥ Fe > Co.[187-190] Recently, five MN_x catalysts (M = Ni, Fe, Co Mn, and Cu) were investigated by Ju and co-workers.[190] At low overpotentials, the first electron transfer to generate a surface adsorbed *COOH species is usually the rate-determining step for CO evolution. The FeN_x catalysts have stronger ΔG_{*COOH}, thus outperforming NiN_4 catalysts. At relatively high overpotentials, the rate-controlling intermediate shifts from COOH* to CO*, in which the FeN_x approached its activity limit for the CO_2RR, because of the strong adsorption of H* intermediate on Fe centers to catalyze the HER process, while the NiN_x sites could continue to increase its CO production rate due to the stronger ΔG_{CO*} than ΔG_{H*}. The CoN_4 catalyst exhibited low CO_2RR activity because of its strong binding energy of H* at all overpotentials. Therefore, Ni[138, 184, 191-197] based MN_x sites with various coordination environments have demonstrated the most efficient CO_2RR to CO with good activity and selectivity. Furthermore, improved CO_2RR performance was achieved on atomically dispersed NiN_4 sites embedded into N, S co-doped graphene (A-Ni-NSG), which was synthesized by a two-step pyrolysis of melamine, L-cysteine, and $Ni(CH_3COO)_2$ precursors (Figure 12a). The CO current density could reach 115 mA cm^{-2} at an applied potential of −1.0 V (Figure 12b). At a

mild overpotential of 0.61 V, the A-Ni-NSG exhibited a high turnover frequency (TOF) of 14,800 h^{-1} with a FE of 97%. In addition, the CO_2 reduction onset potential of A-Ni-NSG was found to be at least 100 mV lower than that of the S-free control (A-Ni-NG). The *in-situ* XAS analysis and DFT calculations indicated that the CO_2RR activity may originate from the charge-transfer from NiN_x sites to CO_2 molecules to form chemically adsorbed $CO_2^{\delta-}$ species (Figure 12c). The S heteroatom likely replaces the N coordination atoms of the NiN_4 moieties via the formation of Ni–S–C bonds, which leads to a non-centrosymmetric configuration, thus facilitating the adsorption of reactants and intermediates onto the active site. Similar to other reactions, the CO_2RR activity of NiN_x sites is affected by the location and coordination. DFT results predicted that several coordinately unsaturated NiN_x moieties, such as divacancy NiN_2V_2,[193] edge-anchored $NiN_2(NH_2)$, and NiN_3 sites[198] should contribute to the high CO_2RR activity of Ni based SACs because they have more optimal adsorption energies for *COOH and *CO and a high activation barrier for H*. Using defect-rich substrates, like microwave exfoliated GO (MEGO), can increase the density of active sites. Sites form readily on the edges of pores, exposed basal-plane edges, and steps of graphene sheets as confirmed by HAADF-STEM images. The obtained catalyst achieved a high Ni loading of 6.9 wt.%, exhibiting a mass activity of 53.6 mA mg^{-1} with a CO selectivity of 92.1% at 0.59 V.

Effect of configuration on activity of SACs. Fe-based SACs have also been experimentally demonstrated as promising candidates for electrocatalytic CO_2RR.[65, 199-202] Some works revealed that the CO_2-to-CO conversion occurs most readily at edge-hosted Fe_{2+2} sites that bridge two

adjacent armchair-like graphitic layers.[65, 202] For instance, the interaction between the reaction intermediates and a model Fe SAC (Fe−N−C) was investigated by combining *in-situ* infrared absorption spectroscopy (ATR-IR) and DFT calculations (Figure 12e).[202] The model Fe−N−C was synthesized by direct pyrolysis of Fe modified ZIF-8 with the optimization of Fe/Zn ratio, heating temperature, and protective atmosphere.[203] STEM (Figure 12d) and XAS analyses confirmed that atomically dispersed Fe atoms were well distributed along the edges of the porous carbon matrix with a FeN_4 configuration, supporting the hypothesis of the edge-host FeN_{2+2} model. The Fe−N−C exhibited a >83% CO FE at a potential range of −0.3 and −0.6 V with a maximum value of 93.5% at −0.5 V, outperforming most N-coordinated Fe SACs.[202] Both the ATR-IR and DFT results (Figure 12f) confirmed that the in-plane FeN_4 sites were easily poisoned by strongly adsorbed CO, while the FeN_{2+2} site could balance the free-energy barriers between CO_2-to-*COOH and *CO-to-CO conversions, and thus should be the real active site for the CO_2RR. The type of coordinated N atoms is another factor to determine the oxidation states of the Fe center. In principle, the Fe^{3+} ions are more active than Fe^{2+} ions due to the enhanced CO_2 adsorption and CO desorption.[28] The operando XAS technology showed that pyrrole-type N promotes the stability of Fe^{3+} more than Fe^{2+}, while the pyridine-type N has an opposite effect.

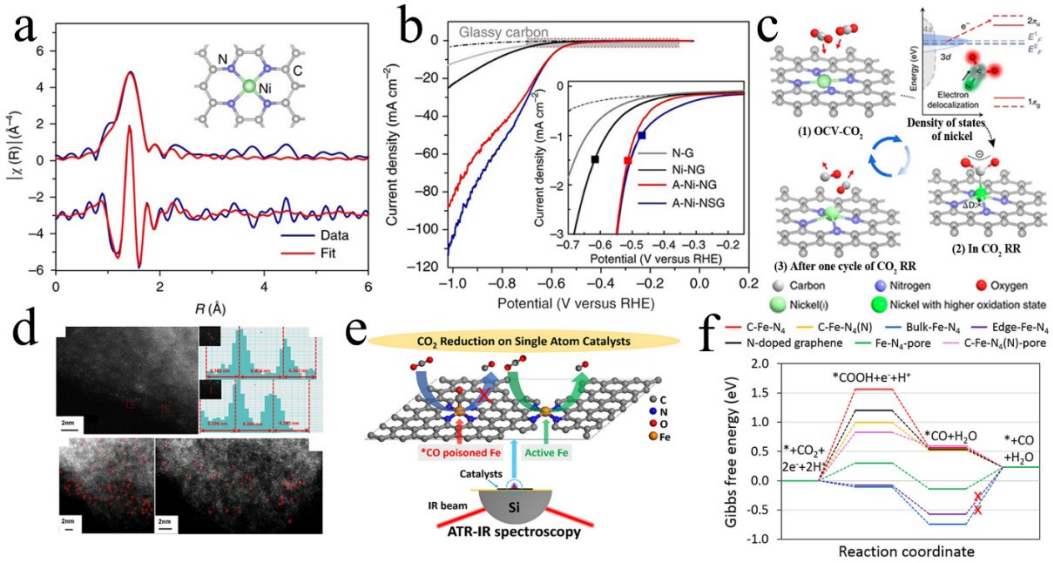

Figure 12. (a) EXAFS spectra and corresponding fitting results for NiN_4 sites. (b) CO2RR LSV curves of S-doped and S-free Ni SACs in CO_2-saturated 0.5 M $KHCO_3$ electrolyte. (c) Schematic of active sites for CO_2RR. Reproduced with permission.[191] Copyright 2018, Nature Publishing Group. (d) HAADF-STEM images showing the Fe sites anchored along the edge of the carbon support. Reproduced with permission.[203] Copyright 2019, Elsevier. (e) The schematic illustration of CO_2RR on FeN_{2+2} sites. (f) Gibbs free energy diagrams of the CO_2RR on different active sites. Reproduced with permission.[202] Copyright 2019, American Chemical Society.

Synergy of dual metal sites. To simultaneously tune the relatively weak adsorption of *COOH on Ni sites and the relatively strong adsorption of CO* on Fe sites, Ni-Fe dual metal sites (Ni/Fe-N-C) have naturally been proposed for CO_2RR (Figure 13).[76] A Ni/Fe-N-C catalyst was synthesized through the pyrolysis of Ni, Fe modified ZIF-8 precursors, where Fe ions anchored onto the nodes and Ni ions were incorporated into cavities of ZIF-8. EXAFS results suggest that Ni/Fe-N-C adopts

a deformed porphyrin-like configuration with the NiN_3 and its neighboring FeN_3 moieties linked by a detectable Ni–Fe bond (Figure 13d–e). The Ni/Fe-N-C exhibited the highest total current density, potential-dependent CO partial current density (j_{CO}), and FE across the entire potential window from -0.4 to –1.0 V, significantly exceeding that of the individual metallic Fe-N-C and Ni-N-C controls (Figure 13f–i). In addition, the Ni/Fe-N-C exhibited a smaller Tafel slope of 96 mV/dec^{-1} and demonstrated excellent stability during 30 h of reaction at –0.7 V. Based on DFT calculations an enhancement mechanism of these Ni/Fe-N-C sites for the CO_2RR was proposed (Figure 13j–l). The geometric structure of dual metal sites enables the CO_2 molecule adsorption on one active site, which facilitates the subsequent dissociation of COOH on the other site.

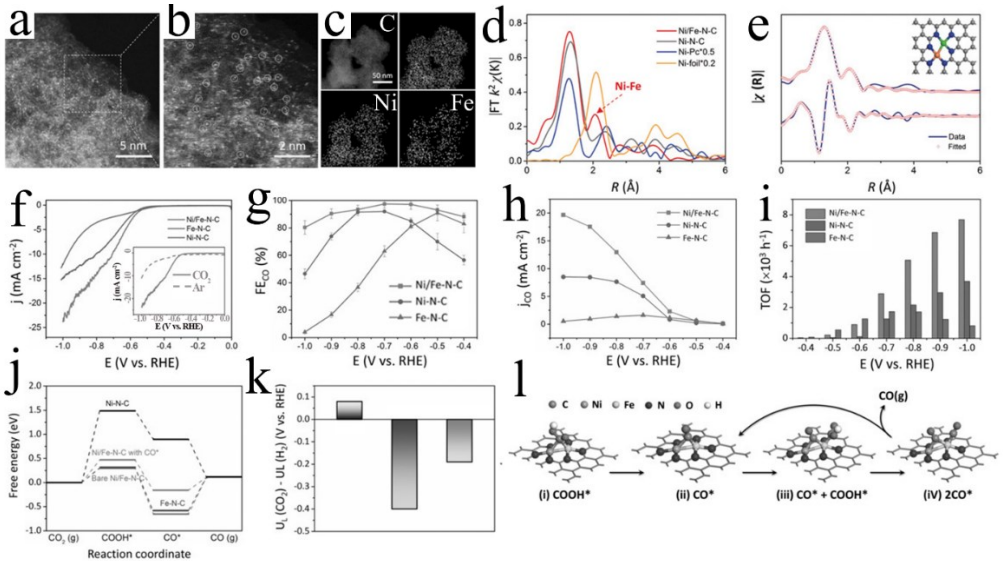

Figure 13. (a–c) HAADF-STEM images and elemental mapping of Ni/Fe-N-C. (d–e) EXAFS spectra and corresponding fitting results for Ni-Fe dual metal sites. The (f) LSV curves, (g) CO FE, (h) j_{CO}, and (i) TOF of Ni/Fe-N-C and the Ni-N-C, Fe-N-C controls in CO_2-saturated 0.5 M $KHCO_3$ electrolyte. (j) Calculated CO_2RR free energy diagrams for different catalysts. (k) Difference in limiting potentials for CO_2RR and

HER of different catalysts. (l)The schematic illustration of suggested catalytic mechanism. Reproduced with permission.[76] Copyright 2019, Wiley-VCH.

Effect of local coordination environment on activity of SACs. Although the intact in-plane CoN_4 moieties were previously suggested to be inert for the CO_2RR due to its high HER activity, several works showed that the CO_2RR activity of Co based SACs could be triggered by engineering the local coordination environment. For example, Wang et al. synthesized a series of CoN_x with a tunable N coordination number by changing the annealing tempurature.[90] Experimental results showed that CO_2RR performance of CoN_x sites largely increased with a decrease in N coordination number from four to two. This is ascribed to the enhanced absorption energies of *COOH on CoN_2 sites, which faciliates the CO_2RR process and inhibits the competive H^* adsorption for the HER. However, a different study observed an opposite activity trend with a higher activity for CoN_4 than $CoN_{4-x}C_x$ sites.[204] In addition, when transition metal centers were embedded into molecular porphyrin rings, without a second C coordination shell, the activity trend changed to Co > Fe > Ni.[65, 205] Thus, the porphyrin Co molecules supported on conductive carbon substrtes[205, 206] or porphyrin Co based covalent organic frameworks[207] also exhibited high CO_2RR performance. The CO selectivity of five-coordinated CoN_5 sites,[205] composed of cobalt porphyrin molecules coordinatively bonded to N-doped carbon, could reach 100% with a high FE of 99%. The activity decreased with a decrease in N coordination number suggesting that the surrounding carbon framework of MN_x sites can also affect the electronic structure and activity of MNx sites.

Other transition metal-based SACs have also been developed for the CO_2RR including ZnN_4[208, 209] and MnN_4Cl[210] sites. Zhang et al. demonstrated that the CO_2RR activity of the MnN_4 moiety could be significantly improved through the introduction of external Cl ligands (Figure 14).[210] Cl-coordinated MnN_4 ((Cl, N)-Mn/G) was synthesized by the pyrolysis of $MnCl_2$ and ethylenediamine at 800 ºC and the Cl-free control sample (N-Mn/G) was obtained by using $Mn(NO_3)_2$ as the precursor. The (Cl, N)-Mn/G exhibited a higher CO_2RR activity than N-Mn/G with a maximum CO FE of 97% and a low overpotential of 0.49 V at 10 mA cm^{-2} (Figure 14b–d). The TOF of (Cl, N)-Mn/G reached 38347 h^{-1} at an overpotential of 0.49 V with considerable stability over 12 h testing. The *in-situ* XAS analysis showed that the (Cl, N)-Mn/G shifted to higher energy after being exposed to CO_2 saturated electrolyte and then shifted back to lower energy during the CO_2RR process at −0.6 V. These results can be explained by the charge transfer from Mn to CO_2 to form a $CO_2^{\delta-}$ species and then ongoing CO_2 reduction, respectively (Figure 14e–f and 14i). DFT caculations further suggest that the role of Cl coordination is to modulate the electronic structure of active Mn centers, reducing the formation energy of intermediates and increases the energy barrier of HER (Figure 14g–h).

The electroreduction of CO_2 to C_1 or C_2 products other than CO has also been studied on these carbon-based SACs. For instance, Ju et al.[211] revealed the mechanistic reaction pathways of the CO_2RR on FeN_4 sites to form methane, formaldehyde, and methanol. Huang et al.[212] prepared atomically dispersed Mo sites on N-doped graphene, which achieved a formate yield of 747 mmol h^{-1} $mg_{cat.}^{-1}$ with an aid of 4 mol% ionic liquid. Jiao et al.[213] demonstrated the formation of C_2

products (e.g., alcohol, ethylene, and ethane) based on atomically dispersed Cu sites on g-C_3N_4, although the FE is low. Recently, Karapinar et al.[214] reported the CO_2 electroreduction on CuN_4 sites to produce ethanol at an FE of 55% in 0.1 M $CsHCO_3$ electrolyte. However, the operando XAS characterization observed the conversion of CuN_4 sites to metallic Cu nanoparticles during the CO_2RR, which are considered the real active sites.

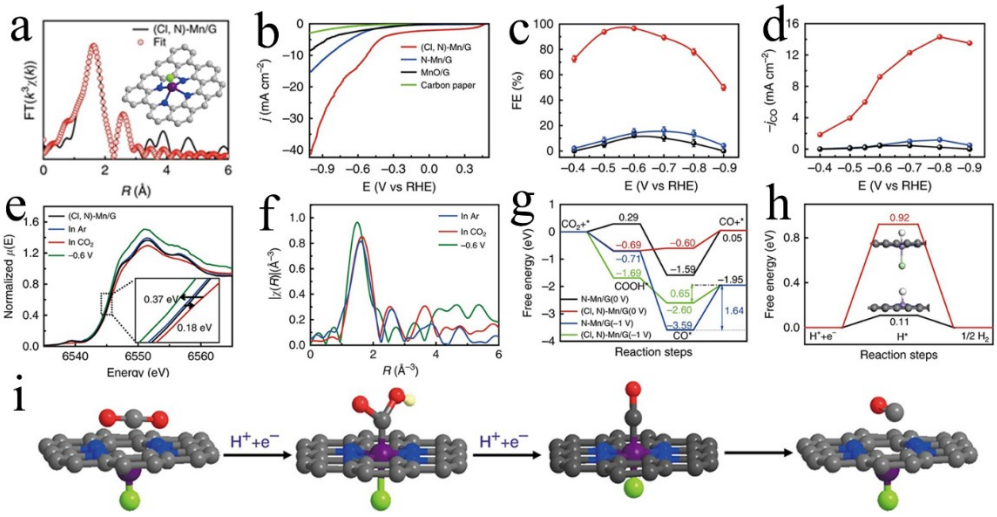

Figure 14. (a) EXAFS results for (Cl, N)-Mn/G. The (b) LSV curves, (c) CO FE, and (d) j_{CO} of (Cl, N)-Mn/G and corresponding controls. (e–f) Normalized XANES of (Cl, N)-Mn/G catalyst under various conditions. (g) Calculated CO_2RR free energy diagrams and (h) calculated HER free energy diagrams of various catalysts. (i) Structural change of the (Cl, N)-Mn/G during electrochemical CO_2RR. The purple, green, blue, red, white, and gray reprents Mn, Cl, N, O, H, and C atoms, respectively. Reproduced with permission.[210] Copyright 2019, Nature Publishing Group.

6.4 The nitrogen reduction reaction

The electrochemical NRR, which converts N_2 to NH_3, is a promising route for achieving clean and

sustainable NH_3 production under ambient conditions.[215, 216] However, current NRR catalysts still suffer from poor activity and selectivity. Different from the Haber–Bosch process, which is believed to involve the initial dissociation of $*N_2$ into two $^*N$, DFT calculations predicted that the NRR process on transition metal surfaces could follow associative mechanisms with a relatively lower reaction barrier such as the enzymatic associative mechanism or the distal/alternating mechanisms.[217, 218] Nevertheless, a minimum overpotential of ~0.4 V is required to promote the electrochemical NRR due to the theoretical limitation of the linearly scaling relationship between the $*N_2H_x$ and $*NH_x$ intermediates for bulk metal surfaces.[219, 220] At this overpotential the competing HER becomes dominant, leading to poor FE for the NRR in most cases. However, coordination-based SACs enable further regulation of the scaling relationships for improved NRR performance. For instance, SACs were found to effectively suppress the HER by weakening the adsorption energy of the H* intermediate. This is because only the top adsorption site is available for SACs, which is different from the case in bulk metal surfaces with several adsorption sites (e.g., top, bridge, and hollow).[221] The unique interaction between metal atoms and the coordination environment could also regulate the linear scaling relation, thus indirectly affecting the NRR activity and selectivity.[47] Consequently, several heteroatom-coordinated SACs have been theoretically identified as promising electrocatalysts for the NRR, such as FeN_x,[222] TiN_4,[221] VN_4,[221] Ti@g-C_3N_4,[223] W@g-C_3N_4,[224] Ru@g-C_3N_4[47] and Ru@GDY.[225]

Recently, the superior NRR performance of coordination-based SACs, compared to their corresponding metal nanoparticles, have been experimentally verified by several works. Based on

a Ru atom modified ZIF-8 precursor, atomically dispersed RuN_x on N-doped carbon has been synthesized to achieve a high yield of 120.9 μg h^{-1} $mg_{cat.}^{-1}$ at −0.2 V with a high FE of 29.6%.[226] In a different work, RuN_x sites on nitrogen-doped carbon embedded with ZrO_2 nanoparticles (Ru@ZrO_2/NC) were synthesized by pyrolysis of Ru ion modified UiO-66 MOFs without acid washing.[227] The Ru@ZrO_2/NC could exhibit higher FE but at a lower NH_3 yield rate compared to Ru@NC without ZrO_2 nanoparticles. DFT results explained that the Ru atoms on N-doped carbon and the Ru atoms on ZrO_2 are likely responsible the high production rate and high selectivity for NH_3, respectively.

PGM-free SACs, including Mo[228] and Fe[229-231] based electrocatalysts, have also been studied for the NRR. In particular, the FeN_4 catalyst exhibited an NH_3 yield rate of 62.9 ± 2.7 μg h^{-1} $mg_{cat.}^{-1}$ in neutral aqueous electrolyte at −0.4 V with a relatively high FE of 18.6 ± 0.8% (Figure 15a–b).[230] It also showed sufficient stability, with only slight activity decay of NH_3 yield over a 24 h potentiostatic test (Figure 15c). DFT calculations determined that the first hydrogenation step ($NN^* + H^+ + e^- \rightarrow *NNH$) is the potential-determining step and that the enzymatic mechanism with the lowest energy barrier should be the most likely reaction pathway on FeN_4 sites. In addition, catalysts poisoned by the SCN^- ion showed an obvious decrease in NRR activity, further confirming that the high NRR activity is due to the FeN_4 sites. However, it should be noted that significant NRR activity of N-doped carbon, as well as the negative effect of Fe atoms on NRR active N_3 sites, has been experimentally demonstrated by other studies.[232, 233] Similar to the ORR and CO_2RR discussed above, engineering of SACs associated with configuration, coordination

environments, dual active sites, and possible synergy with other species would shed light on the rationale to design advanced SACs for improved NRR activity and selectivity.

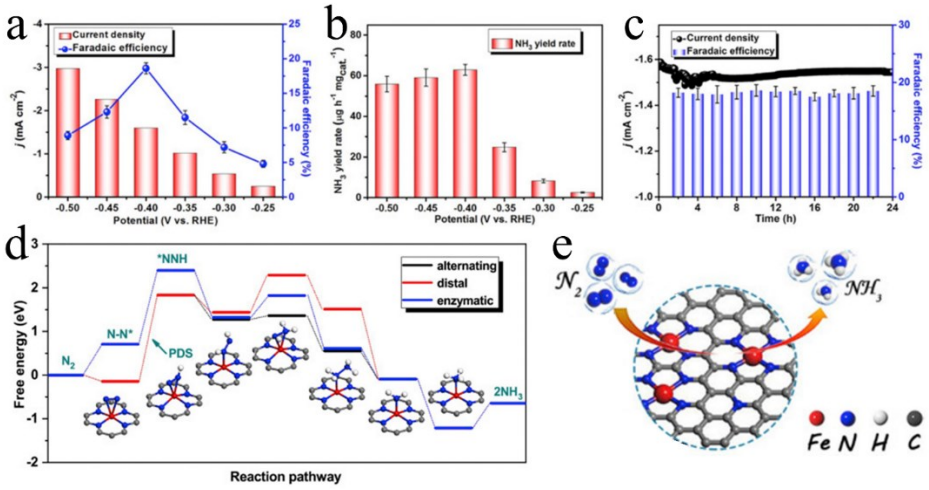

Figure 15. (a) The average current density, FEs and (b) NH_3 yield rate of FeN_4 sample at different potentials. (c) The stability testing for FeN_4 catalyst. (d) Free energy profiles of the NRR on FeN_4 in three proposed pathways. Reproduced with permission.[230] Copyright 2019, Elsevier.

7. Summary and Outlook

Carbon-based and heteroatom-coordinated SACs have exhibited great potential as innovative electrocatalysts for many energy-conversion reactions. Although progress has been made in identifying active sites, enhancing intrinsic activity of SACs through adjusting their electronic and geometric structures still remains a significant challenge. In this review, we discussed recent advancements in engineering local coordination environments of SACs to improve catalytic performance and gain an understanding of the involved mechanisms. Several electronic modulation methods for coordination-based SACs have been experimentally verified such as the

introduction of heteroatom doping, changing the location of single-atoms on various supports, grafting foreign coordination atoms, and the construction of dual metal sites. However, more systematic investigations into the effects of surrounding coordinated-atoms on the intrinsic activity of metal center are still needed. The electronegativity or the withdrawing/donating interaction between metal and the coordination atoms alone may not precisely reflect the structure-activity relationship of carbon-based SACs. An intuitive and accurate descriptor that reflect the structure-activity relationship is highly desired to guide the design of SACs for different reactions. The prerequisite for achieving this goal is the development of more controllable synthesis methods and accurate characterization techniques. Among studied synthesis methods, using chemically and structurally defined MOFs as precursors enabled relatively accurate control of the type and density of the metal centers, but they are relatively difficult to tune with heteroatoms compared to other carbon supports. Some new carbon materials, such as covalent organic frameworks (COFs), are promising alternates to prepare heteroatom modified SACs because of their tunable structures and high thermal stability. In addition, advanced *in-situ* characterization and more accurate DFT calculations are needed to study the nature of active sites and the catalytic mechanisms from both a thermodynamic and kinetics point of view. It should be noted that we primarily focused on modification of local coordination environments of SACs in terms of their intrinsic activity and selectivity instead of the more crucial issue of stability.[234] We admitted that most carbon-based catalysts discussed here would not be suitable for oxidative OER reactions that cause serious carbon corrosion and catalyst degradation. The reason that we still include the OER reactions here

is to shed lights on this challenging reaction is to develop a fundamental understanding of the nature of the metal active sites and reaction pathways. Such fragile carbon-based SACs could become more stable during the OER by integrating highly active and stable oxide supports, especially in less challenging alkaline media.[159, 160, 235-237]

To maximize the synergistic effect between the metal center and its local coordination environment, controllable dispersion methods of singe atom sites into targeted locations on the support, instead of random distributions, are highly desirable. For commercial application, effective synthesis techniques need to be developed for low-cost mass production of SACs with highly reproducible structure and performance. The vacancy trapping methods in liquid-phase, such as photochemical reduction and the sonication-assisted method, seem to be more facile compared to high-temperature pyrolysis. However, the activity and stability of the obtained SAC sites based on these methods should be further investigated. Another major problem is the deactivation or aggregation of single metal atoms caused by carbon corrosion, especially in amorphous carbon structures. On the other hand, single metal atom sites are mainly located on defects and along edges of the support. Therefore, the balance between the density of SAC sites and the graphitization degree of the carbon support should be further explored.[238]

More effort is required to investigate the performance of SAC based electrodes in practical energy conversion devices such as electrolyzers, fuel cells, and metal-air batteries, in which the density of active sites, mass transfer, electron/proton conductivity, and stability of catalysts need to be considered. It should be noted that the review primarily focuses on intrinsic catalytic activity

of single metal sites under a variety of local environments, but less on challenging stability. Also, many carbon-based SACs are produced in powder form and need to be coated onto collectors or films for practical applications. To reduce the weight and volume of the devices, 3D self-supporting electrodes with SACs (e.g., foam graphite and carbon cloth) are highly desired. With continued research efforts, we believe encouraging progress in this field will promote more fundamental research and eventually large-scale implementation in the renewable energy industry sector.

Acknowledgements

G.W. acknowledges the financial support from US Department of Energy, Office of Energy Efficiency and Renewable Energy (EERE), Fuel Cell Technology Office (DE-EE0008075, DE-EE0008076, and DE-EE0008417) along with National Science Foundation (CBET-1604392, 1804326).

Received: ((will be filled in by the editorial staff))
Revised: ((will be filled in by the editorial staff))
Published online: ((will be filled in by the editorial staff))

References

[1] M. C. Argyrou, P. Christodoulides and S. A. Kalogirou, *Renewable Sustainable Energy Rev.* **2018**, 94, 804.

[2] M. Beaudin, H. Zareipour, A. Schellenberglabe and W. Rosehart, *Energy Sustainable Dev.* **2010**, 14, 302.

[3] G. Wu, A. Santandreu, W. Kellogg, S. Gupta, O. Ogoke, H. Zhang, H.-L. Wang and L. Dai, *Nano Energy* **2016**, 29, 83.

[4] R. Abbasi, B. P. Setzler, S. Lin, J. Wang, Y. Zhao, H. Xu, B. Pivovar, B. Tian, X. Chen, G. Wu and Y. Yan, *Adv. Mater.* **2019**, 31.

[5] X. X. Wang, M. T. Swihart and G. Wu, *Nat. Catal.* **2019**, 2, 578.

[6] Y. Li, J. Abbott, Y. Sun, J. Sun, Y. Du, X. Han, G. Wu and P. Xu, *Applied Catalysis B: Environmental* **2019**, 258, 117952.

[7] S. Gupta, W. Kellogg, H. Xu, X. Liu, J. Cho and G. Wu, *Chem. - Asian J.* **2016**, 11, 10.

[8] Y. Peng, B. Lu and S. Chen, *Adv. Mater.* **2018**, 30, e1801995.

[9] Z. W. Seh, J. Kibsgaard, C. F. Dickens, I. Chorkendorff, J. K. Norskov and T. F. Jaramillo, *Science* **2017**, 355.

[10] C. Zhu, S. Fu, Q. Shi, D. Du and Y. Lin, *Angew. Chem. Int. Ed. Engl.* **2017**, 56, 13944.

[11] T. Wang, Q. Zhao, Y. Fu, C. Lei, B. Yang, Z. Li, L. Lei, G. Wu and Y. Hou, *Small Methods* **2019**, 3, 1900210.

[12] J. Di, C. Yan, A. D. Handoko, Z. W. Seh, H. Li and Z. Liu, *Mater. Today* **2018**, 21, 749.

[13] Y. Wang, J. Mao, X. Meng, L. Yu, D. Deng and X. Bao, *Chem. Rev.* **2019**, 119, 1806.

[14] Y. Zhu, W. Peng, Y. Li, G. Zhang, F. Zhang and X. Fan, *Small Methods* **2019**, 3, 1800438.

[15] J. Su, R. Ge, Y. Dong, F. Hao and L. Chen, *J. Mater. Chem. A* **2018**, 6, 14025.

[16] Y. Zhang, L. Guo, L. Tao, Y. Lu and S. Wang, *Small Methods* **2018**, 3, 1800406.

[17] H. J. Qiu, Y. Ito, W. Cong, Y. Tan, P. Liu, A. Hirata, T. Fujita, Z. Tang and M. Chen, *Angew. Chem. Int. Ed.* **2015**, 54, 14031.

[18] L. Zhang, Y. Jia, G. Gao, X. Yan, N. Chen, J. Chen, M. T. Soo, B. Wood, D. Yang, A. Du and X. Yao, *Chem* **2018**, 4, 285.

[19] R. Jiang, L. Li, T. Sheng, G. Hu, Y. Chen and L. Wang, *J. Am. Chem. Soc.* **2018**, 140, 11594.

[20] H. Fei, J. Dong, Y. Feng, C. S. Allen, C. Wan, B. Volosskiy, M. Li, Z. Zhao, Y. Wang, H. Sun, P. An, W. Chen, Z. Guo, C. Lee, D. Chen, I. Shakir, M. Liu, T. Hu, Y. Li, A. I. Kirkland, X. Duan and Y. Huang, *Nat. Catal.* **2018**, 1, 63.

[21] A. Zitolo, V. Goellner, V. Armel, M. T. Sougrati, T. Mineva, L. Stievano, E. Fonda and F. Jaouen, *Nat. Mater.* **2015**, 14, 937.

[22] C. H. Choi, M. Kim, H. C. Kwon, S. J. Cho, S. Yun, H. T. Kim, K. J. Mayrhofer, H. Kim and M. Choi, *Nat. Commun.* **2016**, 7, 10922.

[23] H. Wei, K. Huang, D. Wang, R. Zhang, B. Ge, J. Ma, B. Wen, S. Zhang, Q. Li, M. Lei, C. Zhang, J. Irawan, L. M. Liu and H. Wu, *Nat. Commun.* **2017**, 8, 1490.

[24] S. Wei, A. Li, J. C. Liu, Z. Li, W. Chen, Y. Gong, Q. Zhang, W. C. Cheong, Y. Wang, L. Zheng, H. Xiao, C. Chen, D. Wang, Q. Peng, L. Gu, X. Han, J. Li and Y. Li, *Nat Nanotechnol* **2018**, 13, 856.

[25] H. T. Chung, D. A. Cullen, D. Higgins, B. T. Sneed, E. F. Holby, K. L. More and P. Zelenay, *Science* **2017**, 357, 479.

[26] A. D. Handoko, F. Wei, Jenndy, B. S. Yeo and Z. W. Seh, *Nat. Catal.* **2018**, 1, 922.

[27] Q. Jia, E. Liu, L. Jiao, S. Pann and S. Mukerjee, *Adv. Mater.* **2019**, 31, e1805157.

[28] J. Gu, C. S. Hsu, L. Bai, H. M. Chen and X. Hu, *Science* **2019**, 364, 1091.

[29] Q. Li, W. Chen, H. Xiao, Y. Gong, Z. Li, L. Zheng, X. Zheng, W. Yan, W. C. Cheong, R. Shen, N. Fu, L. Gu, Z. Zhuang, C. Chen, D. Wang, Q. Peng, J. Li and Y. Li, *Adv. Mater.* **2018**, 30, e1800588.

[30] U. I. Kramm, L. Ni and S. Wagner, *Adv. Mater.* **2019**, 31, e1805623.

[31] T. Mineva, I. Matanovic, P. Atanassov, M.-T. Sougrati, L. Stievano, M. Clémancey, A. Kochem, J.-M. Latour and F. Jaouen, *ACS Catalysis* **2019**, 9, 9359.

[32] A. D. Handoko, S. N. Steinmann and Z. W. Seh, *Nanoscale Horizons* **2019**, 4, 809.

[33] A. J. Medford, A. Vojvodic, J. S. Hummelshøj, J. Voss, F. Abild-Pedersen, F. Studt, T. Bligaard, A. Nilsson and J. K. Nørskov, *Journal of Catalysis* **2015**, 328, 36.

[34] J. K. Nørskov, J. Rossmeisl, A. Logadottir, L. Lindqvist, J. R. Kitchin, T. Bligaard and H. Jónsson, *J. Phys. Chem. B* **2004**, 108, 17886.

[35] A. G. Saputro and H. Kasai, *Phys. Chem. Chem. Phys.* **2015**, 17, 3059.

[36] S. Kattel, P. Atanassov and B. Kiefer, *Phys. Chem. Chem. Phys.* **2014**, 16, 13800.

[37] G. Gao, S. Bottle and A. Du, *Catalysis Science & Technology* **2018**, 8, 996.

[38] G. Zhu, F. Liu, Y. Wang, Z. Wei and W. Wang, *Phys. Chem. Chem. Phys.* **2019**, 21, 12826.

[39] B. Lu, T. J. Smart, D. Qin, J. E. Lu, N. Wang, L. Chen, Y. Peng, Y. Ping and S. Chen, *Chem. Mater.* **2017**, 29, 5617.

[40] N. Ramaswamy, U. Tylus, Q. Jia and S. Mukerjee, *J. Am. Chem. Soc.* **2013**, 135, 15443.

[41] H. Xu, D. Cheng, D. Cao and X. C. Zeng, *Nat. Catal.* **2018**, 1, 339.

[42] M. G. Kibria, J. P. Edwards, C. M. Gabardo, C. T. Dinh, A. Seifitokaldani, D. Sinton and E. H. Sargent, *Adv. Mater.* **2019**, 31, e1807166.

[43] Z. Tian, C. Priest and L. Chen, *Advanced Theory and Simulations* **2018**, 1, 1800004.

[44] S. Back, J. Lim, N. Y. Kim, Y. H. Kim and Y. Jung, *Chem. Sci.* **2017**, 8, 1090.

[45] L. Gong, D. Zhang, C. Y. Lin, Y. Zhu, Y. Shen, J. Zhang, X. Han, L. Zhang and Z. Xia, *Adv. Energy Mater.* **2019**, DOI: 10.1002/aenm.201902625, 1902625.

[46] M. D. Hossain, Z. Liu, M. Zhuang, X. Yan, G.-L. Xu, C. A. Gadre, A. Tyagi, I. H. Abidi, C.-J. Sun, H. Wong, A. Guda, Y. Hao, X. Pan, K. Amine and Z. Luo, *Adv. Energy Mater.* **2019**, 9, 1803689.

[47] X. Liu, Y. Jiao, Y. Zheng, M. Jaroniec and S. Z. Qiao, *J. Am. Chem. Soc.* **2019**, 141, 9664.

[48] L. Osmieri, A. H. A. Monteverde Videla, P. Ocón and S. Specchia, *J. Phys. Chem. C* **2017**, 121, 17796.

[49] H. Peng, F. Liu, X. Liu, S. Liao, C. You, X. Tian, H. Nan, F. Luo, H. Song, Z. Fu and P. Huang, *ACS Catalysis* **2014**, 4, 3797.

[50] Y. Chen, S. Ji, S. Zhao, W. Chen, J. Dong, W. C. Cheong, R. Shen, X. Wen, L. Zheng, A. I. Rykov, S. Cai, H. Tang, Z. Zhuang, C. Chen, Q. Peng, D. Wang and Y. Li, *Nat. Commun.* **2018**, 9, 5422.

[51] D. Liu, X. Li, S. Chen, H. Yan, C. Wang, C. Wu, Y. A. Haleem, S. Duan, J. Lu, B. Ge, P. M. Ajayan, Y. Luo, J. Jiang and L. Song, *Nature Energy* **2019**, 4, 512.

[52] Q. K. Li, X. F. Li, G. Zhang and J. Jiang, *J. Am. Chem. Soc.* **2018**, 140, 15149.

[53] L. Zhang, J. Fischer, Y. Jia, X. Yan, W. Xu, X. Wang, J. Chen, D. Yang, H. Liu, L. Zhuang, M. Hankel, D. J. Searles, K. Huang, S. Feng, C. L. Brown and X. Yao, *J. Am. Chem. Soc.* **2018**, 140, 10757.

[54] Y. Hou, M. Qiu, M. G. Kim, P. Liu, G. Nam, T. Zhang, X. Zhuang, B. Yang, J. Cho, M. Chen, C. Yuan, L. Lei and X. Feng, *Nat. Commun.* **2019**, 10, 1392.

[55] Y. Han, Y. Wang, R. Xu, W. Chen, L. Zheng, A. Han, Y. Zhu, J. Zhang, H. Zhang, J. Luo, C. Chen, Q. Peng, D. Wang and Y. Li, *Energy & Environmental Science* **2018**, 11, 2348.

[56] L. Zhao, R. He, K. T. Rim, T. Schiros, K. S. Kim, H. Zhou, C. Gutierrez, S. P. Chockalingam, C. J. Arguello, L. Palova, D. Nordlund, M. S. Hybertsen, D. R. Reichman, T. F. Heinz, P. Kim, A. Pinczuk, G. W. Flynn and A. N. Pasupathy, *Science* **2011**, 333, 999.

[57] H. B. Yang, J. Miao, S. F. Hung, J. Chen, H. B. Tao, X. Wang, L. Zhang, R. Chen, J. Gao, H. M. Chen, L. Dai and B. Liu, *Science advances* **2016**, 2, e1501122.

[58] L. Yang, D. Cheng, H. Xu, X. Zeng, X. Wan, J. Shui, Z. Xiang and D. Cao, *Proc. Natl. Acad. Sci. U S A*

2018, 115, 6626.

[59] M. Lefevre, E. Proietti, F. Jaouen and J. P. Dodelet, *Science* **2009**, 324, 71.

[60] H. Zhang, S. Hwang, M. Wang, Z. Feng, S. Karakalos, L. Luo, Z. Qiao, X. Xie, C. Wang, D. Su, Y. Shao and G. Wu, *J. Am. Chem. Soc.* **2017**, 139, 14143.

[61] X. X. Wang, D. A. Cullen, Y. T. Pan, S. Hwang, M. Wang, Z. Feng, J. Wang, M. H. Engelhard, H. Zhang, Y. He, Y. Shao, D. Su, K. L. More, J. S. Spendelow and G. Wu, *Adv. Mater.* **2018**, 30, 1706758.

[62] S. Kattel and G. Wang, *J. Phys. Chem. Lett.* **2014**, 5, 452.

[63] Y. He, S. Hwang, D. A. Cullen, M. A. Uddin, L. Langhorst, B. Li, S. Karakalos, A. J. Kropf, E. C. Wegener, J. Sokolowski, M. Chen, D. Myers, D. Su, K. L. More, G. Wang, S. Litster and G. Wu, *Energy. Environ. Sci.* **2019**, 12, 250.

[64] X. Fu, N. Li, B. Ren, G. Jiang, Y. Liu, F. M. Hassan, D. Su, J. Zhu, L. Yang, Z. Bai, Z. P. Cano, A. Yu and Z. Chen, *Adv. Energy Mater.* **2019**, 9, 1803737.

[65] F. Pan, H. Zhang, K. Liu, D. Cullen, K. More, M. Wang, Z. Feng, G. Wang, G. Wu and Y. Li, *ACS Catalysis* **2018**, 8, 3116.

[66] M. J. Workman, A. Serov, L.-k. Tsui, P. Atanassov and K. Artyushkova, *ACS Energy Lett.* **2017**, 2, 1489.

[67] D. Zhang, W. Chen, Z. Li, Y. Chen, L. Zheng, Y. Gong, Q. Li, R. Shen, Y. Han, W. C. Cheong, L. Gu and Y. Li, *Chem. Commun.* **2018**, 54, 4274.

[68] J. Wang, Z. Huang, W. Liu, C. Chang, H. Tang, Z. Li, W. Chen, C. Jia, T. Yao, S. Wei, Y. Wu and Y. Li, *J. Am. Chem. Soc.* **2017**, 139, 17281.

[69] G. Zhang, Y. Jia, C. Zhang, X. Xiong, K. Sun, R. Chen, W. Chen, Y. Kuang, L. Zheng, H. Tang, W. Liu, J. Liu, X. Sun, W.-F. Lin and H. Dai, *Energy. Environ. Sci.* **2019**, 12, 1317.

[70] J. Wang, W. Liu, G. Luo, Z. Li, C. Zhao, H. Zhang, M. Zhu, Q. Xu, X. Wang, C. Zhao, Y. Qu, Z. Yang, T. Yao, Y. Li, Y. Lin, Y. Wu and Y. Li, *Energy & Environmental Science* **2018**, 11, 3375.

[71] Z. Lu, B. Wang, Y. Hu, W. Liu, Y. Zhao, R. Yang, Z. Li, J. Luo, B. Chi, Z. Jiang, M. Li, S. Mu, S. Liao, J. Zhang and X. Sun, *Angew. Chem. Int. Ed.* **2019**, 131, 2648.

[72] D. Liu, B. Wang, H. Li, S. Huang, M. Liu, J. Wang, Q. Wang, J. Zhang and Y. Zhao, *Nano Energy* **2019**, 58, 277.

[73] B. Wang, J. Zou, X. Shen, Y. Yang, G. Hu, W. Li, Z. Peng, D. Banham, A. Dong and D. Zhao, *Nano Energy* **2019**, 63, 103851.

[74] L. Zhang, Y. Jia, H. Liu, L. Zhuang, X. Yan, C. Lang, X. Wang, D. Yang, K. Huang, S. Feng and X. Yao, *Angew. Chem. Int. Ed. Engl.* **2019**, 58, 9404.

[75] X. Liu, Y. Jiao, Y. Zheng, K. Davey and S.-Z. Qiao, *J. Mater. Chem. A* **2019**, 7, 3648.

[76] W. Ren, X. Tan, W. Yang, C. Jia, S. Xu, K. Wang, S. C. Smith and C. Zhao, *Angew. Chem. Int. Ed. Engl.* **2019**, 58, 6972.

[77] Q. Jia, N. Ramaswamy, H. Hafiz, U. Tylus, K. Strickland, G. Wu, B. Barbiellini, A. Bansil, E. F. Holby, P. Zelenay and S. Mukerjee, *ACS Nano* **2015**, 9, 12496.

[78] E. F. Holby and C. D. Taylor, *Sci. Rep.* **2015**, 5, 9286.

[79] Y. Wang, Y. J. Tang and K. Zhou, *J. Am. Chem. Soc.* **2019**, 141, 14115.

[80] H. C. Kwon, M. Kim, J. P. Grote, S. J. Cho, M. W. Chung, H. Kim, D. H. Won, A. R. Zeradjanin, K. J. J. Mayrhofer, M. Choi, H. Kim and C. H. Choi, *J. Am. Chem. Soc.* **2018**, 140, 16198.

[81] Y. Lin, P. Liu, E. Velasco, G. Yao, Z. Tian, L. Zhang and L. Chen, *Adv. Mater.* **2019**, 31, e1808193.

[82] X. Zeng, J. Shui, X. Liu, Q. Liu, Y. Li, J. Shang, L. Zheng and R. Yu, *Adv. Energy Mater.* **2018**, 8, 1701345.

[83] X. P. Yin, H. J. Wang, S. F. Tang, X. L. Lu, M. Shu, R. Si and T. B. Lu, *Angew. Chem. Int. Ed.* **2018**, 57, 9382.

[84] K. Qu, Y. Zheng, Y. Jiao, X. Zhang, S. Dai and S.-Z. Qiao, *Adv. Energy Mater.* **2017**, 7, 1602068.

[85] Z. Qiao, H. Zhang, S. Karakalos, S. Hwang, J. Xue, M. Chen, D. Su and G. Wu, *Applied Catalysis B: Environmental* **2017**, 219, 629.

[86] H. Zhang, H. Osgood, X. Xie, Y. Shao and G. Wu, *Nano Energy* **2017**, 31, 331.

[87] H. Zhang, J. Li, Q. Tan, L. Lu, Z. Wang and G. Wu, *Chem. - Eur. J.* **2018**, 24, 18137.

[88] P. Yin, T. Yao, Y. Wu, L. Zheng, Y. Lin, W. Liu, H. Ju, J. Zhu, X. Hong, Z. Deng, G. Zhou, S. Wei and Y. Li, *Angew. Chem. Int. Ed.* **2016**, 55, 10800.

[89] H. Zhang, S. Ding, S. Hwang, X. Zhao, D. Su, H. Xu, H. Yang and G. Wu, *J. Electrochem. Soc.* **2019**, 166, F3116.

[90] X. Wang, Z. Chen, X. Zhao, T. Yao, W. Chen, R. You, C. Zhao, G. Wu, J. Wang, W. Huang, J. Yang, X. Hong, S. Wei, Y. Wu and Y. Li, *Angew. Chem.* **2018**, 130, 1962.

[91] Q. Liu, X. Liu, L. Zheng and J. Shui, *Angew. Chem. Int. Ed. Engl.* **2018**, 57, 1204.

[92] H. Zhang, H. T. Chung, D. A. Cullen, S. Wagner, U. I. Kramm, K. L. More, P. Zelenay and G. Wu, *Energy. Environ. Sci.* **2019**, 12, 2548.

[93] H. Wang, F. X. Yin, N. Liu, R. H. Kou, X. B. He, C. J. Sun, B. H. Chen, D. J. Liu and H. Q. Yin, *Adv. Funct. Mater.* **2019**, 29, 1901531.

[94] W. J. Jiang, L. Gu, L. Li, Y. Zhang, X. Zhang, L. J. Zhang, J. Q. Wang, J. S. Hu, Z. Wei and L. J. Wan, *J. Am. Chem. Soc.* **2016**, 138, 3570.

[95] C. Lei, Y. Wang, Y. Hou, P. Liu, J. Yang, T. Zhang, X. Zhuang, M. Chen, B. Yang, L. Lei, C. Yuan, M. Qiu and X. Feng, *Energy. Environ. Sci.* **2019**, 12, 149.

[96] X. Ao, W. Zhang, Z. Li, L. Lv, Y. Ruan, H.-H. Wu, W.-H. Chiang, C. Wang, M. Liu and X. C. Zeng, *J. Mater. Chem. A* **2019**, 7, 11792.

[97] K. Liu, G. Wu and G. Wang, *J. Phys. Chem. C* **2017**, 121, 11319.

[98] Z. Lionet, S. Nishijima, T. H. Kim, Y. Horiuchi, S. W. Lee and M. Matsuoka, *Dalton Trans* **2019**, 48, 13953.

[99] S. L. Zhang, B. Y. Guan and X. W. D. Lou, *Small* **2019**, 15, e1805324.

[100] L. Zheng, Y. Dong, B. Chi, Z. Cui, Y. Deng, X. Shi, L. Du and S. Liao, *Small* **2019**, 15, e1803520.

[101] Y. Qu, B. Chen, Z. Li, X. Duan, L. Wang, Y. Lin, T. Yuan, F. Zhou, Y. Hu, Z. Yang, C. Zhao, J. Wang, C. Zhao, Y. Hu, G. Wu, Q. Zhang, Q. Xu, B. Liu, P. Gao, R. You, W. Huang, L. Zheng, L. Gu, Y. Wu and Y. Li, *J. Am. Chem. Soc.* **2019**, 141, 4505.

[102] Y. Qu, Z. Li, W. Chen, Y. Lin, T. Yuan, Z. Yang, C. Zhao, J. Wang, C. Zhao, X. Wang, F. Zhou, Z. Zhuang, Y. Wu and Y. Li, *Nat. Catal.* **2018**, 1, 781.

[103] D. Deng, X. Chen, L. Yu, X. Wu, Q. Liu, Y. Liu, H. Yang, H. Tian, Y. Hu, P. Du, R. Si, J. Wang, X. Cui, H. Li, J. Xiao, T. Xu, J. Deng, F. Yang, P. N. Duchesne, P. Zhang, J. Zhou, L. Sun, J. Li, X. Pan and X. Bao, *Science advances* **2015**, 1, e1500462.

[104] X. Cui, J. Xiao, Y. Wu, P. Du, R. Si, H. Yang, H. Tian, J. Li, W. H. Zhang, D. Deng and X. Bao, *Angew. Chem. Int. Ed.* **2016**, 55, 6708.

[105] Y. Xue, B. Huang, Y. Yi, Y. Guo, Z. Zuo, Y. Li, Z. Jia, H. Liu and Y. Li, *Nat. Commun.* **2018**, 9, 1460.

[106] L. Zhang, L. Han, H. Liu, X. Liu and J. Luo, *Angew. Chem. Int. Ed. Engl.* **2017**, 56, 13694.

[107] W. Bi, X. Li, R. You, M. Chen, R. Yuan, W. Huang, X. Wu, W. Chu, C. Wu and Y. Xie, *Adv. Mater.* **2018**, 30, e1706617.

[108] Z. Zhang, Y. Chen, L. Zhou, C. Chen, Z. Han, B. Zhang, Q. Wu, L. Yang, L. Du, Y. Bu, P. Wang, X. Wang, H. Yang and Z. Hu, *Nat. Commun.* **2019**, 10, 1657.

[109] T. Li, J. Liu, Y. Song and F. Wang, *ACS Catalysis* **2018**, 8, 8450.

[110] K. Huang, L. Zhang, T. Xu, H. Wei, R. Zhang, X. Zhang, B. Ge, M. Lei, J. Y. Ma, L. M. Liu and H. Wu, *Nat. Commun.* **2019**, 10, 606.

[111] X. Wan, X. Liu, Y. Li, R. Yu, L. Zheng, W. Yan, H. Wang, M. Xu and J. Shui, *Nat. Catal.* **2019**, 2, 259.

[112] V. Yarlagadda, M. K. Carpenter, T. E. Moylan, R. S. Kukreja, R. Koestner, W. Gu, L. Thompson and A. Kongkanand, *ACS Energy Lett.* **2018**, 3, 618.

[113] R. Chenitz, U. I. Kramm, M. Lefèvre, V. Glibin, G. Zhang, S. Sun and J.-P. Dodelet, *Energy & Environmental Science* **2018**, 11, 365.

[114] F. Jaouen, M. Lefevre, J. P. Dodelet and M. Cai, *J. Phys. Chem. B* **2006**, 110, 5553.

[115] S. H. Lee, J. Kim, D. Y. Chung, J. M. Yoo, H. S. Lee, M. J. Kim, B. S. Mun, S. G. Kwon, Y. E. Sung and T. Hyeon, *J. Am. Chem. Soc.* **2019**, 141, 2035.

[116] Y. Chen, Z. Li, Y. Zhu, D. Sun, X. Liu, L. Xu and Y. Tang, *Adv. Mater.* **2019**, 31, e1806312.

[117] T. Sun, S. Zhao, W. Chen, D. Zhai, J. Dong, Y. Wang, S. Zhang, A. Han, L. Gu, R. Yu, X. Wen, H. Ren, L. Xu, C. Chen, Q. Peng, D. Wang and Y. Li, *Proc. Natl. Acad. Sci. U S A* **2018**, 115, 12692.

[118] W. Chen, J. Pei, C. T. He, J. Wan, H. Ren, Y. Zhu, Y. Wang, J. Dong, S. Tian, W. C. Cheong, S. Lu, L. Zheng, X. Zheng, W. Yan, Z. Zhuang, C. Chen, Q. Peng, D. Wang and Y. Li, *Angew. Chem. Int. Ed.* **2017**, 56, 16086.

[119] X. Zhao, P. Pachfule, S. Li, T. Langenhahn, M. Ye, G. Tian, J. Schmidt and A. Thomas, *Chem. Mater.* **2019**, 31, 3274.

[120] C. Zhu, Q. Shi, B. Z. Xu, S. Fu, G. Wan, C. Yang, S. Yao, J. Song, H. Zhou, D. Du, S. P. Beckman, D. Su and Y. Lin, *Adv. Energy Mater.* **2018**, DOI: 10.1002/aenm.201801956, 1801956.

[121] C. Cheng, S. Li, Y. Xia, L. Ma, C. Nie, C. Roth, A. Thomas and R. Haag, *Adv. Mater.* **2018**, DOI: 10.1002/adma.201802669, e1802669.

[122] H. Shen, E. Gracia-Espino, J. Ma, K. Zang, J. Luo, L. Wang, S. Gao, X. Mamat, G. Hu, T. Wagberg and S. Guo, *Angew. Chem. Int. Ed.* **2017**, 56, 13800.

[123] W. Liu, L. Zhang, X. Liu, X. Liu, X. Yang, S. Miao, W. Wang, A. Wang and T. Zhang, *J. Am. Chem. Soc.* **2017**, 139, 10790.

[124] Y. Zhu, T. Cao, C. Cao, J. Luo, W. Chen, L. Zheng, J. Dong, J. Zhang, Y. Han, Z. Li, C. Chen, Q. Peng, D. Wang and Y. Li, *ACS Catalysis* **2018**, DOI: 10.1021/acscatal.8b02624.

[125] J. Wu, H. Zhou, Q. Li, M. Chen, J. Wan, N. Zhang, L. Xiong, S. Li, B. Y. Xia, G. Feng, M. Liu and L. Huang, *Adv. Energy Mater.* **2019**, 9, 1900149.

[126] S. Li, C. Cheng, X. Zhao, J. Schmidt and A. Thomas, *Angew. Chem. Int. Ed. Engl.* **2018**, 57, 1856.

[127] B. Q. Li, C. X. Zhao, J. N. Liu and Q. Zhang, *Adv. Mater.* **2019**, 31.

[128] Z. Qiao, S. Hwang, X. Li, C. Wang, W. Samarakoon, S. Karakalos, D. Li, M. Chen, Y. He, M. Wang, Z. Liu, G. Wang, H. Zhou, Z. Feng, D. Su, J. S. Spendelow and G. Wu, *Energy. Environ. Sci.* **2019**, 12, 2830.

[129] M. Chen, S. Hwang, J. Li, S. Karakalos, K. Chen, Y. He, S. Mukherjee, D. Su and G. Wu, *Nanoscale* **2018**, 10.

[130] X. X. Wang, S. Hwang, Y. T. Pan, K. Chen, Y. He, S. Karakalos, H. Zhang, J. S. Spendelow, D. Su and G. Wu, *Nano Lett.* **2018**, 18, 4163.

[131] J. Liu, M. Jiao, L. Lu, H. M. Barkholtz, Y. Li, Y. Wang, L. Jiang, Z. Wu, D. J. Liu, L. Zhuang, C. Ma, J. Zeng, B. Zhang, D. Su, P. Song, W. Xing, W. Xu, Y. Wang, Z. Jiang and G. Sun, *Nat. Commun.* **2017**, 8, 15938.

[132] J. Liu, M. Jiao, B. Mei, Y. Tong, Y. Li, M. Ruan, P. Song, G. Sun, L. Jiang, Y. Wang, Z. Jiang, L. Gu, Z. Zhou and W. Xu, *Angew. Chem.* **2018**, 131, 1175.

[133] M. Chen, Y. He, J. S. Spendelow and G. Wu, *ACS Energy Lett.* **2019**, 4, 1619.

[134] J. Li, M. Chen, D. A. Cullen, S. Hwang, M. Wang, B. Li, K. Liu, S. Karakalos, M. Lucero, H. Zhang, C. Lei, H. Xu, G. E. Sterbinsky, Z. Feng, D. Su, K. L. More, G. Wang, Z. Wang and G. Wu, *Nat. Catal.* **2018**, 1, 935.

[135] Q. Li, H. Pan, D. Higgins, R. Cao, G. Zhang, H. Lv, K. Wu, J. Cho and G. Wu, *Small* **2015**, 11, 1443.

[136] J. Li, H. Zhang, W. Samarakoon, W. Shan, D. Cullen, S. Karakalos, M. Chen, D. Gu, K. More, G. Wang, Z. Feng, Z. Wang and G. Wu, *Angew. Chem. Int. Ed. Engl.* **2019**, DOI: 10.1002/anie.201909312.

[137] C. Hu and L. Dai, *Adv. Mater.* **2019**, 31, e1804672.

[138] W. Zheng, C. Guo, J. Yang, F. He, B. Yang, Z. Li, L. Lei, J. Xiao, G. Wu and Y. Hou, *Carbon* **2019**, 150, 52.

[139] Y.-C. Wang, Y.-J. Lai, L. Song, Z.-Y. Zhou, J.-G. Liu, Q. Wang, X.-D. Yang, C. Chen, W. Shi, Y.-P. Zheng, M. Rauf and S.-G. Sun, *Angew. Chem. Int. Ed.* **2015**, 127, 10045.

[140] E. Luo, M. Xiao, Y. Wang, J. Ge, C. Liu and W. Xing, *ChemCatChem* **2018**, 10, 3653.

[141] Y. Mun, S. Lee, K. Kim, S. Kim, S. Lee, J. W. Han and J. Lee, *J. Am. Chem. Soc.* **2019**, 141, 6254.

[142] K. Yuan, S. Sfaelou, M. Qiu, D. Lützenkirchen-Hecht, X. Zhuang, Y. Chen, C. Yuan, X. Feng and U. Scherf, *ACS Energy Lett.* **2018**, 3, 252.

[143] Y. Yang, K. Mao, S. Gao, H. Huang, G. Xia, Z. Lin, P. Jiang, C. Wang, H. Wang and Q. Chen, *Adv. Mater.* **2018**, 30, e1801732.

[144] Q. Li, R. Cao, J. Cho and G. Wu, *Adv. Energy Mater.* **2014**, 4, 1301415.

[145] Q. He, Q. Li, S. Khene, X. Ren, F. E. López-Suárez, D. Lozano-Castelló, A. Bueno-López and G. Wu, *J. Phys. Chem. C* **2013**, 117, 8697.

[146] W. Gao, D. Havas, S. Gupta, Q. Pan, N. He, H. Zhang, H.-L. Wang and G. Wu, *Carbon* **2016**, 102, 346.

[147] G. Wu, *Frontiers in Energy* **2017**, 11, 286.

[148] G. Wu, K. L. More, C. M. Johnston and P. Zelenay, *Science* **2011**, 332.

[149] G. Wu and P. Zelenay, *Acc. Chem. Res.* **2013**, 46, 1878.

[150] X. Fu, P. Zamani, J. Y. Choi, F. M. Hassan, G. Jiang, D. C. Higgins, Y. Zhang, M. A. Hoque and Z. Chen, *Adv. Mater.* **2017**, 29, 1604456.

[151] Y. Ye, F. Cai, H. Li, H. Wu, G. Wang, Y. Li, S. Miao, S. Xie, R. Si, J. Wang and X. Bao, *Nano Energy* **2017**, 38, 281.

[152] C. Zhang, Y. C. Wang, B. An, R. Huang, C. Wang, Z. Zhou and W. Lin, *Adv. Mater.* **2017**, 29, 1604556.

[153] G. Wu, N. H. Mack, W. Gao, S. Ma, R. Zhong, J. Han, J. K. Baldwin and P. Zelenay, *ACS Nano* **2012**, 6, 9764.

[154] G. Wu, K. L. More, P. Xu, H.-L. Wang, M. Ferrandon, A. J. Kropf, D. J. Myers, S. Ma and P. Zelenay, *Chem. Commun.* **2013**, 49, 3291.

[155] X. X. Wang, V. Prabhakaran, Y. He, Y. Shao and G. Wu, *Adv. Mater.* **2019**, 31, e1805126.

[156] K. Liu, Z. Qiao, S. Hwang, Z. Liu, H. Zhang, D. Su, H. Xu, G. Wu and G. Wang, *Applied Catalysis B:*

Environmental **2019**, 243, 195.

[157] M. Xiao, H. Zhang, Y. Chen, J. Zhu, L. Gao, Z. Jin, J. Ge, Z. Jiang, S. Chen, C. Liu and W. Xing, *Nano Energy* **2018**, 46, 396.

[158] C. Lei, H. Chen, J. Cao, J. Yang, M. Qiu, Y. Xia, C. Yuan, B. Yang, Z. Li, X. Zhang, L. Lei, J. Abbott, Y. Zhong, X. Xia, G. Wu, Q. He and Y. Hou, *Adv. Energy Mater.* **2018**, 8.

[159] C. Lei, S. Lyu, J. Si, B. Yang, Z. Li, Z. Wen, L. Lei, J. Abbott, G. Wu and Y. Hou, *ChemCatChem*, doi:10.1002/cctc.201901707.

[160] J. Guan, Z. Duan, F. Zhang, S. D. Kelly, R. Si, M. Dupuis, Q. Huang, J. Q. Chen, C. Tang and C. Li, *Nat. Catal.* **2018**, DOI: 10.1038/s41929-018-0158-6.

[161] X. Li, P. Cui, W. Zhong, J. Li, X. Wang, Z. Wang and J. Jiang, *Chem. Commun.* **2016**, 52, 13233.

[162] Y. Zheng, Y. Jiao, Y. Zhu, Q. Cai, A. Vasileff, L. H. Li, Y. Han, Y. Chen and S. Z. Qiao, *J. Am. Chem. Soc.* **2017**, 139.

[163] D. Liu, S. Ding, C. Wu, W. Gan, C. Wang, D. Cao, Z. u. Rehman, Y. Sang, S. Chen, X. Zheng, Y. Wang, B. Ge and L. Song, *J. Mater. Chem. A* **2018**, 6.

[164] C. Wu, X. Zhang, Z. Xia, M. Shu, H. Li, X. Xu, R. Si, A. I. Rykov, J. Wang, S. Yu, S. Wang and G. Sun, *Journal of Materials Chemistry A* **2019**, 7, 14001.

[165] S. V. Devaguptapu, S. Hwang, S. Karakalos, S. Zhao, S. Gupta, D. Su, H. Xu and G. Wu, *ACS Applied Materials & Interfaces* **2017**, 9.

[166] L. Yang, L. Shi, D. Wang, Y. Lv and D. Cao, *Nano Energy* **2018**, 50, 691.

[167] W. Zang, A. Sumboja, Y. Ma, H. Zhang, Y. Wu, S. Wu, H. Wu, Z. Liu, C. Guan, J. Wang and S. J. Pennycook, *ACS Catalysis* **2018**, 8, 8961.

[168] P. Chen, T. Zhou, L. Xing, K. Xu, Y. Tong, H. Xie, L. Zhang, W. Yan, W. Chu, C. Wu and Y. Xie, *Angew. Chem. Int. Ed.* **2017**, 56.

[169] Y. Pan, S. Liu, K. Sun, X. Chen, B. Wang, K. Wu, X. Cao, W. C. Cheong, R. Shen, A. Han, Z. Chen, L. Zheng, J. Luo, Y. Lin, Y. Liu, D. Wang, Q. Peng, Q. Zhang, C. Chen and Y. Li, *Angew. Chem. Int. Ed.* **2018**, 57, 8614.

[170] L. Ma, S. Chen, Z. Pei, Y. Huang, G. Liang, F. Mo, Q. Yang, J. Su, Y. Gao, J. A. Zapien and C. Zhi, *ACS Nano* **2018**, 12, 1949.

[171] Y. Guo, P. Yuan, J. Zhang, Y. Hu, I. S. Amiinu, X. Wang, J. Zhou, H. Xia, Z. Song, Q. Xu and S. Mu, *ACS Nano* **2018**, 12, 1894.

[172] J. Zhang, M. Zhang, Y. Zeng, J. Chen, L. Qiu, H. Zhou, C. Sun, Y. Yu, C. Zhu and Z. Zhu, *Small* **2019**, 15, e1900307.

[173] H. Wei, H. Wu, K. Huang, B. Ge, J. Ma, J. Lang, D. Zu, M. Lei, Y. Yao, W. Guo and H. Wu, *Chem. Sci.* **2019**, 10, 2830.

[174] N. Cheng, S. Stambula, D. Wang, M. N. Banis, J. Liu, A. Riese, B. Xiao, R. Li, T. K. Sham, L. M. Liu, G. A. Botton and X. Sun, *Nat. Commun.* **2016**, 7, 13638.

[175] J. Durst, A. Siebel, C. Simon, F. Hasché, J. Herranz and H. A. Gasteiger, *Energy. Environ. Sci.* **2014**, 7, 2255.

[176] W. Sheng, M. Myint, J. G. Chen and Y. Yan, *Energy. Environ. Sci.* **2013**, 6, 1509.

[177] B. Lu, L. Guo, F. Wu, Y. Peng, J. E. Lu, T. J. Smart, N. Wang, Y. Z. Finfrock, D. Morris, P. Zhang, N. Li, P. Gao, Y. Ping and S. Chen, *Nat. Commun.* **2019**, 10, 631.

[178] Y. Peng, W. Pan, N. Wang, J. E. Lu and S. Chen, *ChemSusChem* **2018**, 11, 130.

[179] H. Fei, J. Dong, M. J. Arellano-Jimenez, G. Ye, N. Dong Kim, E. L. Samuel, Z. Peng, Z. Zhu, F. Qin, J. Bao, M. J. Yacaman, P. M. Ajayan, D. Chen and J. M. Tour, *Nat. Commun.* **2015**, 6, 8668.

[180] J.-D. Yi, R. Xu, G.-L. Chai, T. Zhang, K. Zang, B. Nan, H. Lin, Y.-L. Liang, J. Lv, J. Luo, R. Si, Y.-B. Huang and R. Cao, *J. Mater. Chem. A* **2019**, 7, 1252.

[181] H. Fei, J. Dong, C. Wan, Z. Zhao, X. Xu, Z. Lin, Y. Wang, H. Liu, K. Zang, J. Luo, S. Zhao, W. Hu, W. Yan, I. Shakir, Y. Huang and X. Duan, *Adv. Mater.* **2018**, 30, e1802146.

[182] L. Cao, Q. Luo, W. Liu, Y. Lin, X. Liu, Y. Cao, W. Zhang, Y. Wu, J. Yang, T. Yao and S. Wei, *Nat. Catal.* **2018**, 2, 134.

[183] W. Chen, J. Pei, C. T. He, J. Wan, H. Ren, Y. Wang, J. Dong, K. Wu, W. C. Cheong, J. Mao, X. Zheng, W. Yan, Z. Zhuang, C. Chen, Q. Peng, D. Wang and Y. Li, *Adv. Mater.* **2018**, 30, e1800396.

[184] T. Wang, H. Xie, M. Chen, A. D'Aloia, J. Cho, G. Wu and Q. Li, *Nano Energy* **2017**, 42, 69.

[185] Y. Jiao, Y. Zheng, K. Davey and S.-Z. Qiao, *Nature Energy* **2016**, 1, 16130.

[186] X. Wang, Q. Zhao, B. Yang, Z. Li, Z. Bo, K. H. Lam, N. M. Adli, L. Lei, Z. Wen, G. Wu and Y. Hou, *J. Mater. Chem. A* **2019**, DOI: 10.1039/c9ta09681g.

[187] Y. Cheng, S. Zhao, B. Johannessen, J. P. Veder, M. Saunders, M. R. Rowles, M. Cheng, C. Liu, M. F. Chisholm, R. De Marco, H. M. Cheng, S. Z. Yang and S. P. Jiang, *Adv. Mater.* **2018**, 30, e1706287.

[188] X.-M. Hu, H. H. Hval, E. T. Bjerglund, K. J. Dalgaard, M. R. Madsen, M.-M. Pohl, E. Welter, P. Lamagni, K. B. Buhl, M. Bremholm, M. Beller, S. U. Pedersen, T. Skrydstrup and K. Daasbjerg, *ACS Catalysis* **2018**, 8, 6255.

[189] F. Pan, W. Deng, C. Justiniano and Y. Li, *Applied Catalysis B: Environmental* **2018**, 226, 463.

[190] W. Ju, A. Bagger, G. P. Hao, A. S. Varela, I. Sinev, V. Bon, B. Roldan Cuenya, S. Kaskel, J. Rossmeisl and P. Strasser, *Nat. Commun.* **2017**, 8, 944.

[191] H. B. Yang, S.-F. Hung, S. Liu, K. Yuan, S. Miao, L. Zhang, X. Huang, H.-Y. Wang, W. Cai, R. Chen, J. Gao, X. Yang, W. Chen, Y. Huang, H. M. Chen, C. M. Li, T. Zhang and B. Liu, *Nature Energy* **2018**, 3, 140.

[192] C. Zhao, X. Dai, T. Yao, W. Chen, X. Wang, J. Wang, J. Yang, S. Wei, Y. Wu and Y. Li, *J. Am. Chem. Soc.* **2017**, 139, 8078.

[193] C. Yan, H. Li, Y. Ye, H. Wu, F. Cai, R. Si, J. Xiao, S. Miao, S. Xie, F. Yang, Y. Li, G. Wang and X. Bao, *Energy. Environ. Sci.* **2018**, 11, 1204.

[194] S. Zhao, Y. Cheng, J.-P. Veder, B. Johannessen, M. Saunders, L. Zhang, C. Liu, M. F. Chisholm, R. De Marco, J. Liu, S.-Z. Yang and S. P. Jiang, *ACS Applied Energy Materials* **2018**, DOI: 10.1021/acsaem.8b00903.

[195] X. Li, W. Bi, M. Chen, Y. Sun, H. Ju, W. Yan, J. Zhu, X. Wu, W. Chu, C. Wu and Y. Xie, *J. Am. Chem. Soc.* **2017**, 139, 14889.

[196] P. Lu, Y. Yang, J. Yao, M. Wang, S. Dipazir, M. Yuan, J. Zhang, X. Wang, Z. Xie and G. Zhang, *Applied Catalysis B: Environmental* **2019**, 241, 113.

[197] F. Pan, H. Zhang, Z. Liu, D. A. Cullen, K. Liu, K. L. More, G. Wu, G. Wang and Y. Li, *J. Mater. Chem. A* **2019**, DOI: 10.1039/c9ta08862h.

[198] Y. Cheng, S. Zhao, H. Li, S. He, J.-P. Veder, B. Johannessen, J. Xiao, S. Lu, J. Pan, M. F. Chisholm, S.-Z. Yang, C. Liu, J. G. Chen and S. P. Jiang, *Applied Catalysis B: Environmental* **2019**, 243, 294.

[199] H. Zhong, F. Meng, Q. Zhang, K. Liu and X. Zhang, *Nano Research* **2019**, 12, 2318.

[200] T. N. Huan, N. Ranjbar, G. Rousse, M. Sougrati, A. Zitolo, V. Mougel, F. Jaouen and M. Fontecave, *ACS Catalysis* **2017**, 7, 1520.

[201] C. Zhang, S. Yang, J. Wu, M. Liu, S. Yazdi, M. Ren, J. Sha, J. Zhong, K. Nie, A. S. Jalilov, Z. Li, H. Li, B. I. Yakobson, Q. Wu, E. Ringe, H. Xu, P. M. Ajayan and J. M. Tour, *Adv. Energy Mater.* **2018**, 8, 1703487.

[202] X. Qin, S. Zhu, F. Xiao, L. Zhang and M. Shao, *ACS Energy Lett.* **2019**, 4, 1778.

[203] F. Xiao, G.-L. Xu, C.-J. Sun, M. Xu, W. Wen, Q. Wang, M. Gu, S. Zhu, Y. Li, Z. Wei, X. Pan, J. Wang, K. Amine and M. Shao, *Nano Energy* **2019**, 61, 60.

[204] Z. Geng, Y. Cao, W. Chen, X. Kong, Y. Liu, T. Yao and Y. Lin, *Applied Catalysis B: Environmental* **2019**, 240, 234.

[205] Y. Pan, R. Lin, Y. Chen, S. Liu, W. Zhu, X. Cao, W. Chen, K. Wu, W. C. Cheong, Y. Wang, L. Zheng, J. Luo, Y. Lin, Y. Liu, C. Liu, J. Li, Q. Lu, X. Chen, D. Wang, Q. Peng, C. Chen and Y. Li, *J. Am. Chem. Soc.* **2018**, 140, 4218.

[206] X. Zhang, Z. Wu, X. Zhang, L. Li, Y. Li, H. Xu, X. Li, X. Yu, Z. Zhang, Y. Liang and H. Wang, *Nat. Commun.* **2017**, 8, 14675.

[207] C. S. Diercks, S. Lin, N. Kornienko, E. A. Kapustin, E. M. Nichols, C. Zhu, Y. Zhao, C. J. Chang and O. M. Yaghi, *J. Am. Chem. Soc.* **2018**, 140, 1116.

[208] Z. Chen, K. Mou, S. Yao and L. Liu, *ChemSusChem* **2018**, 11, 2944.

[209] F. Yang, P. Song, X. Liu, B. Mei, W. Xing, Z. Jiang, L. Gu and W. Xu, *Angew. Chem.* **2018**, 130, 12483.

[210] B. Zhang, J. Zhang, J. Shi, D. Tan, L. Liu, F. Zhang, C. Lu, Z. Su, X. Tan, X. Cheng, B. Han, L. Zheng and J. Zhang, *Nat. Commun.* **2019**, 10, 2980.

[211] W. Ju, A. Bagger, X. Wang, Y. Tsai, F. Luo, T. Möller, H. Wang, J. Rossmeisl, A. S. Varela and P. Strasser, *ACS Energy Lett.* **2019**, 4, 1663.

[212] P. Huang, M. Cheng, H. Zhang, M. Zuo, C. Xiao and Y. Xie, *Nano Energy* **2019**, 61, 428.

[213] Y. Jiao, Y. Zheng, P. Chen, M. Jaroniec and S. Z. Qiao, *J. Am. Chem. Soc.* **2017**, 139, 18093.

[214] D. Karapinar, N. T. Huan, N. Ranjbar Sahraie, J. Li, D. Wakerley, N. Touati, S. Zanna, D. Taverna, L. H. Galvao Tizei, A. Zitolo, F. Jaouen, V. Mougel and M. Fontecave, *Angew. Chem. Int. Ed.* **2019**, 58, 15098.

[215] K. Ithisuphalap, H. Zhang, L. Guo, Q. Yang, H. Yang and G. Wu, *Small Methods* **2019**, 3, 1800352.

[216] G.-F. Chen, S. Ren, L. Zhang, H. Cheng, Y. Luo, K. Zhu, L.-X. Ding and H. Wang, *Small Methods* **2019**, 3, 1800337.

[217] X. F. Li, Q. K. Li, J. Cheng, L. Liu, Q. Yan, Y. Wu, X. H. Zhang, Z. Y. Wang, Q. Qiu and Y. Luo, *J. Am. Chem. Soc.* **2016**, 138, 8706.

[218] X. Cui, C. Tang and Q. Zhang, *Advanced Energy Materials* **2018**, 8, 1800369.

[219] J. H. Montoya, C. Tsai, A. Vojvodic and J. K. Norskov, *ChemSusChem* **2015**, 8, 2180.

[220] C. J. van der Ham, M. T. Koper and D. G. Hetterscheid, *Chem. Soc. Rev.* **2014**, 43, 5183.

[221] C. Choi, S. Back, N.-Y. Kim, J. Lim, Y.-H. Kim and Y. Jung, *ACS Catalysis* **2018**, 8, 7517.

[222] X. Guo, J. Gu, X. Hu, S. Zhang, Z. Chen and S. Huang, *Catal. Today* **2019**, DOI: 10.1016/j.cattod.2019.06.014.

[223] X. Chen, X. Zhao, Z. Kong, W.-J. Ong and N. Li, *J. Mater. Chem. A* **2018**, 6, 21941.

[224] Z. Chen, J. Zhao, C. R. Cabrera and Z. Chen, *Small Methods* **2018**, 3, 1800368.

[225] D. Ma, Z. Zeng, L. Liu, X. Huang and Y. Jia, *J. Phys. Chem. C* **2019**, 123, 19066.

[226] Z. Geng, Y. Liu, X. Kong, P. Li, K. Li, Z. Liu, J. Du, M. Shu, R. Si and J. Zeng, *Adv. Mater.* **2018**, DOI:

10.1002/adma.201803498, e1803498.

[227] H. Tao, C. Choi, L.-X. Ding, Z. Jiang, Z. Han, M. Jia, Q. Fan, Y. Gao, H. Wang, A. W. Robertson, S. Hong, Y. Jung, S. Liu and Z. Sun, *Chem* **2019**, 5, 204.

[228] L. Han, X. Liu, J. Chen, R. Lin, H. Liu, F. Lu, S. Bak, Z. Liang, S. Zhao, E. Stavitski, J. Luo, R. R. Adzic and H. L. Xin, *Angew. Chem. Int. Ed.* **2019**, 58, 2321.

[229] Y. Wang, X. Cui, J. Zhao, G. Jia, L. Gu, Q. Zhang, L. Meng, Z. Shi, L. Zheng, C. Wang, Z. Zhang and W. Zheng, *ACS Catalysis* **2018**, 9, 336.

[230] F. Lü, S. Zhao, R. Guo, J. He, X. Peng, H. Bao, J. Fu, L. Han, G. Qi, J. Luo, X. Tang and X. Liu, *Nano Energy* **2019**, 61, 420.

[231] C. He, Z.-Y. Wu, L. Zhao, M. Ming, Y. Zhang, Y. Yi and J.-S. Hu, *ACS Catalysis* **2019**, 9, 7311.

[232] S. Mukherjee, D. A. Cullen, S. Karakalos, K. Liu, H. Zhang, S. Zhao, H. Xu, K. L. More, G. Wang and G. Wu, *Nano Energy* **2018**, 48, 217.

[233] Y. Liu, Y. Su, X. Quan, X. Fan, S. Chen, H. Yu, H. Zhao, Y. Zhang and J. Zhao, *ACS Catalysis* **2018**, 8, 1186.

[234] Y. Shao, J.-P. Dodelet, G. Wu and P. Zelenay, *Adv. Mater.* **2019**, 31.

[235] H. Osgood, S. V. Devaguptapu, H. Xu, J. Cho and G. Wu, *Nano Today* **2016**, 11.

[236] S. Gupta, L. Qiao, S. Zhao, H. Xu, Y. Lin, S. V. Devaguptapu, X. Wang, M. T. Swihart and G. Wu, *Adv. Energy Mater.* **2016**, 6.

[237] S. Gupta, S. Zhao, X. X. Wang, S. Hwang, S. Karakalos, S. V. Devaguptapu, S. Mukherjee, D. Su, H. Xu and G. Wu, *ACS Catalysis* **2017**, 7.

[238] X. Wang, Q. Li, H. Pan, Y. Lin, Y. Ke, H. Sheng, M. T. Swihart and G. Wu, *Nanoscale* **2015**, 7, 20290.

Carbon-based heteroatom-coordinated single-atom catalysts are promising candidates for energy-conversion related electrocatalysts. This review summarizes recent advances in engineering the carbon-based heteroatom-coordinated single metal site catalysts for energy-related electrochemical reactions, including oxygen reduction reaction (ORR), hydrogen evolution reaction (HER), oxygen evolution reaction (OER), CO_2 reduction reaction (CO_2RR), and nitrogen reduction reaction (NRR).

Keywords: electrocatalysis, energy conversion, single-atom site catalysts, heteroatom doping, coordination environment

Y. Zhu, J. Sokolowski, X. Song, Y. He, Yi Mei, and Gang Wu**

Engineering Local Coordination Environments of Atomically Dispersed and Heteroatom-coordinated Single Metal Site Electrocatalysts for Clean Energy-Conversion

ToC